

FACULTY OF PHYSICS. MATHEMATICS AND OPTOMETRY

Annamarija Trausa

Probing metal and metal oxide nanowire physical properties using *in situ* microscopy nanomanipulation techniques

SUMMARY OF DOCTORAL THESIS

Submitted for the degree of Doctor of Science (Ph.D.) in Natural Sciences
Field of Physics and Astronomy
Subfield of Materials Physics

The doctoral thesis was carried out at the Institute of Solid State Physics of University of Latvia and Institute of Physics of University of Tartu, from year 2020 to 2024.

Form of the thesis: dissertation in Physics and Astronomy, subfield of Materials Physics

Supervisor: *Dr. phys.* **Edgars Butanovs**, University of Latvia, Institute of Solid State Physics, Latvia.

Reviewers:

- 1) Dr. phys. Jana Andzane, University of Latvia, Latvia
- 2) Dr. Tadas Malinauskas, University of Vilnius, Lithuania
- 3) Dr. Dirk Dietzel, Justus-Liebig-Universität Giessen, Germany

The thesis is available at the Library of the University of Latvia, Raina blvd. 19.

Chairman of the Doctoral Committee: Dr. habil. phys. Uldis Rogulis

Secretary of the Doctoral Committee: Sintija Silina

ABSTRACT

This Dissertation is dedicated to understanding the mechanical properties and thermal behaviour of one-dimensional nanostructures by implementing diverse nanomanipulation techniques in combination with electron and atomic force microscopies. Key findings include the first-time demonstration of post-synthesis kinking in non-metallic nanowires, determination of the elastic modulus of individual $\beta\text{-}Ga_2O_3$ nanowires using two different techniques, and exploring Au and Ag nanowire thermal stability under different heating schemes, including Au nanowire heat-induced fragmentation for surface enhanced Raman spectroscopy substrate application. These investigations contribute to a better understanding of the mechanical properties and thermal behaviour of nanowires, highlighting the importance of different manipulation methods and substrate interactions in determining their properties and potential applications.

Keywords: nanowires; nanomanipulations; scanning electron microscopy; atomic force microscopy; heat-induced fragmentation

TABLE OF CONTENTS

1. IN'	TRODUCTION	6
1.1.	MOTIVATION	6
1.2.	OBJECTIVE AND TASKS	7
1.3.	THESES TO BE DEFENDED	7
1.4.	SCIENTIFIC NOVELTY	8
1.5.	CONTRIBUTION OF THE AUTHOR	8
1.6.	APPROBATION OF THE DISSERTATION	9
2. NA	NOMATERIALS AND THEIR PROPERTIES	10
2.1.	NANOMATERIALS	10
2.2.	Nanowires	10
2.3.	STRUCTURE	13
2.4.	MECHANICAL PROPERTIES	14
2.5.	THERMAL PROPERTIES	16
3. EX	PERIMENTAL TECHNIQUES	18
3.1.	MICROSCOPY TECHNIQUES	18
3.2.	NANOMANIPULATIONS	19
4. MATERIALS AND METHODS		21
4.1.	CUO NANOWIRE SYNTHESIS AND CHARACTERISATION	21
4.2.	Ga_2O_3 nanowire synthesis and characterisation	21
4.3.	AU NANOWIRE SYNTHESIS AND CHARACTERISATION	22
4.4.	AG NANOWIRE CHARACTERIZATION	23
5. RE	SULTS AND DISCUSSION	24
5.1.	POST-SYNTHESIS KINKING IN CUO NANOWIRES	24
5.2.	MECHANICAL PROPERTIES OF GA ₂ O ₃ NANOWIRES	31
5.3.	HEAT-INDUCED FRAGMENTATION AND ADHESIVE BEHAVIOR	OUR
OF AU NANOV	VIRES	36
5.4.	HEAT-INDUCED MORPHOLOGICAL CHANGES IN AG NANOV	VIRES
	40	
CONCL	USIONS	46
PARTIC	CIPATION IN SUMMER SCHOOLS AND	
	ES	
	ENCES	
ACKNOWLEDGEMENTS5		

1. INTRODUCTION

1.1. Motivation

Nanomaterials, characterized by at least one dimension between 1 and 100 nm, represent a remarkable class of materials that exhibit unique properties and behaviours distinct from their bulk counterparts [1]. Through the fabrication of nanostructures, such as nanowires (NWs), nanomaterials achieve exceptionally large surface areas, enabling the development of materials with outstanding mechanical, optical, electrical, magnetic, and catalytic capabilities [2]. These properties make nanomaterials essential across diverse industries, including biomedicine, electronics, energy, and materials science, driving the rapid advancement of nanotechnology [3].

Furthermore, NWs have attracted significant interest due to their potential applications in various fields, including nanophotonics, electronics, and sensing [4]. The emergence of flexible electronics has underscored the importance of characterizing NWs to ensure the reliability of the flexible electronic components [5]. Understanding the mechanical properties and thermal stability of NWs is important for their effective use in these applications, necessitating precise characterization techniques [6]. From a fundamental physics perspective, the small size and excellent material properties of NWs make them an ideal platform for investigating new physical phenomena at nanoscale which are challenging to observe in other types of materials [7].

Despite the challenges posed by their small-scale size, methods such as scanning electron microscopy (SEM) and atomic force microscopy (AFM) manipulations offer valuable insights into NW properties [8]. These imaging and manipulation techniques allow to closely examine the structural and mechanical characteristics of NWs, revealing details that are critical for understanding their behaviour. Additionally, networks of NWs, including those composed of noble metals like Au and Ag, exhibit intriguing phenomena such as spheroidization due to Rayleigh instability induced by heating [9]. Theoretical models and experimental studies aimed at exploring the complexities of NW behaviour are essential for advancing our understanding of nanomaterials and driving innovations in nanotechnology and materials science [10].

Metal and metal oxide NW compounds such as Ga₂O₃, CuO, Ag, and Au have physical properties that are not thoroughly studied and fully understood yet. Investigating these characteristics is essential for the materials applicability thus this Dissertation focuses on studying the physical properties of these promising NW compounds to uncover their full potential and enable their use in diverse applications.

1.2. Objective and tasks

The main **objective** of this work is to investigate mechanical and thermal behaviours of selected material NWs using electron microscopy nanomanipulation techniques and heating experiments.

The **tasks** have been outlined as follows:

- 1. To study post-synthesis kink formation in CuO NWs with different mechanical nanomanipulation techniques.
- 2. To determine elastic modulus of β -Ga₂O₃ NWs using *in situ* SEM resonance and three-point bending in AFM;
- 3. To investigate the behaviour of heat-induced fragmentation in Au and Ag NWs under different heating schemes.
- 4. To study the differences in heat-induced fragmentation between freestanding Ag NWs and those adhered to a substrate.

1.3. Theses to be defended

- Post-synthesis kinking of single-crystal CuO nanowires can be induced by mechanical manipulations, with deformation twinning along the (110) crystal plane being the underlying mechanism.
- 2. The elastic modulus of β -Ga₂O₃ nanowires was determined using in situ scanning electron microscopy resonance and three-point bending atomic force microscopy techniques, yielding mean values of 34.5 GPa and 75.8 GPa, respectively. Variations in cross-section geometry and different growth directions contribute to the scattering of these elastic modulus values. These methods are reliable for accurate nanowire elastic modulus measurement required for nanodevice engineering.
- 3. The heat-induced fragmentation of Au and Ag nanowires is affected by the manner in which temperature is raised, with fewer splits per nanowire length observed during rapid heating cycles, while direct temperature elevation results in more splits per nanowire length. The controlled fragmentation of Au nanowires results in periodic, costeffective, and easily producible substrates for surface-enhanced Raman scattering.
- 4. Fragmentation of suspended Ag nanowire parts is dominant when heated incrementally in rapid cycles, while fragmentation of the adhered parts primarily occurs under direct temperature elevation, which is caused by mechanical stresses that arise in nanowires as an interplay between thermal expansion and frictional forces. Ag nanowires remain

morphologically stable up to 275°C, thus Ag nanowire networks can be safely used up to 275°C, beyond which fragmentation begins to occur.

1.4. Scientific novelty

This Dissertation focuses on understanding the mechanical behaviour of nanostructures through manipulation techniques and observing how heat affects the morphology of nanostructures, providing insights into their behaviour in different conditions. The following findings can be highlighted:

- 1. Demonstration of post-synthesis kinking in covalent NWs through various manipulation scenarios;
- 2. Determination of the elastic modulus of individual β-Ga₂O₃ NWs through two different techniques: *in situ* SEM resonance and three-point bending in AFM;
- 3. Use of heat-induced fragmentation in Au NWs for surface-enhanced Raman scattering (SERS) substrate applications, supplemented by AFM manipulations to confirm nanoparticle (NP) adhesion to the substrate;
- 4. Investigation how heat treatment affects pentagonal Ag NWs partially in contact with a substrate, revealing contrasting behaviours between suspended and adhered parts during heating, showing substrate-induced effects beyond Rayleigh instability.

1.5. Contribution of the Author

The direct contribution of the Author is as follows: in **Paper I**, the Author characterised and manipulated CuO NWs using a scanning electron microscope. The Author engaged in discussions and contributed to the analysis of the observed experimental data. Furthermore, in **Paper II**, the Author wrote the main body of the article, characterised NWs and conducted *in situ* SEM resonance measurements, analysed the data and was the corresponding author. Similarly, in **Paper III**, the Author wrote the main body of the article, conducted SEM characterization, and analysed the data, also conducted sample heating experiments with various heating schemes and was the corresponding author of the article. Lastly, in **Paper IV**, the Author contributed to transmission electron microscopy and SEM measurements and participated in heating experiments.

Interpretation of all the obtained results was performed in collaboration with Author's supervisor and all colleagues who were co-authors in aforementioned scientific papers.

1.6. Approbation of the Dissertation

Publications included in Dissertation:

- I Vlassov, S., Oras, S., **Trausa, A.**, Tiirats, T., Butanovs, E., Polyakov, B., Zadin, V. and Kyritsakis, A. Reshaping covalent nanowires by exploiting an unexpected plasticity mediated by deformation twinning. *Small*, 2024, 20(1), p.2304614.
- **II Trausa, A.**, Oras, S., Vlassov, S., Antsov, M., Tiirats, T., Kyritsakis, A., Polyakov, B., Butanovs, E. Elastic Modulus of β -Ga₂O₃ Nanowires Measured by Resonance and Three-Point Bending Techniques. *Beilstein J. Nanotechnol.*, 2024, *15*, 704–712.
- **III Trausa, A.**, Tipaldi, C.F., Ignatane, L., Polyakov, B., Oras, S., Butanovs, E., Vanags, E. and Smits, K. Heat-Induced Fragmentation and Adhesive Behaviour of Gold Nanowires for Surface-Enhanced Raman Scattering Substrates. *ChemEngineering*, 2024, 8(1), p.15.
- **IV** Damerchi, E., Oras, S., Butanovs, E., Liivlaid, A., Antsov, M., Polyakov, B., **Trausa, A.**, Zadin, V., Kyritsakis, A., Vidal, L., Mougin, K., Pikker, S., Sergei Vlassov, S. Heat-induced morphological changes in silver nanowires deposited on a patterned silicon substrate. *Beilstein J. Nanotechnol.* 2024, *15*, p.435.

Publications not included in Dissertation:

Polyakov, B., Kadiwala, K., Butanovs, E., Dipane, L., **Trausa, A.**, Bocharov, D. and Vlassov, S. Synthesis of ZnS/Al₂O₃/TaSe₂ Core/Shell Nanowires Using Thin Ta Metal Film Precursor. *ChemEngineering*, 2024, 8(1), p.25.

Vanags, E., Bite, I., Ignatane, L., Ignatans, R., **Trausa, A.**, Tipaldi, C.F., Vilks, K. and Smits, K. Zinc Oxide Tetrapods Doped with Silver Nanoparticles as a Promising Substrate for the Detection of Biomolecules via Surface-Enhanced Raman Spectroscopy. *ChemEngineering*, 2024, 8(1), p.19.

Manika, I., Krasta, T., Maniks, J., Bikse, L., Susinska, J., Leimane, M., **Trausa**, **A.**, Grants, R. and Popov, A.I. Effect of ion-induced nuclear reactions on structure modification and radiolysis in LiF irradiated by 410 MeV 36S ions. *Optical Materials*, 2023, *138*, p.113686.

2. NANOMATERIALS AND THEIR PROPERTIES

2.1. Nanomaterials

Nanomaterials are a remarkable class of materials defined by at least one dimension between 1 and 100 nm [1]. Their creation results in exceptionally large surface areas and unique mechanical, optical, electrical, magnetic, and catalytic properties that differ significantly from their bulk counterparts. By precisely adjusting their size, shape, synthesis parameters, and functionalization, the properties of nanomaterials can be tailored for specific applications [2]. Consequently, these materials are utilized across diverse industries, including biomedicine, agriculture, electronics, energy, coatings, food engineering, telecommunications, transportation, cosmetics, and mechanical engineering. The scientific field of nanotechnology encompasses the development, engineering, and use of nanostructures and has garnered significant attention due to the innovative applications of nanomaterials for future industrial advancements [3].

Nanostructures are categorized based on their dimensions: zero-dimensional (0D), one-dimensional (1D), two-dimensional (2D), and three-dimensional (3D) [11]. Zero-dimensional materials, such as quantum dots and nanoparticles, have all dimensions within the nanoscale range [3,12]. One-dimensional materials, like NWs and nanotubes, have two dimensions within the nanoscale range and can be embedded within other materials [3,13]. Two-dimensional nanomaterials, such as coatings and nanosheets, have plate-like forms with two dimensions outside the nanoscale range [3,14]. Moreover, three-dimensional nanomaterials are not limited to the nanoscale in any dimension and include dispersed nanoparticles and multi-nanolayers, often featuring interfaces formed by 0D, 1D, and 2D components [3,15].

2.2. Nanowires

NWs are a class of nanostructures characterized by their significant length compared to their width, attracting extensive research interest over the past few decades [16,17]. They can be metallic, semiconducting, or dielectric, with applications in plasmonic and photonic waveguiding, light production, sensing, nanophotonics, and electronics [18-20]. NWs are ideal for investigating new physical phenomena at the nanoscale due to their small size and excellent material properties [21].

Considerable research focuses on understanding NW growth at the atomic scale, managing dimensions, crystal structure, composition, and growth

patterns [19]. NWs are commonly fabricated using "bottom-up" methods, such as solution growth, template-guided synthesis, and the vapor-liquid-solid (VLS) process, which are more cost-effective than "top-down" methods like conventional lithography [22]. In the VLS process, metal nanoparticle catalysts play a crucial role by adsorbing gaseous precursors and guiding the growth of crystalline material through stages of alloying, nucleation, and growth [19]. Furthermore, adjusting growth conditions allows for compositional and structural manipulation, although challenges persist in achieving certain desired structures and maintaining optimal growth parameters [23].

Expected to be key in future electrical and optoelectronic devices, semiconducting NWs offer a platform for investigating nanoscale phenomena [7]. Metal oxide NWs represent a pivotal group of semiconductor NWs due to their significant electrical, optical, and chemical sensing properties [24]. Recent advances have highlighted monoclinic gallium oxide (β -Ga₂O₃) [25-27] due to its outstanding properties [28] such as chemical stability and ultra-wide band gap (4.4 - 4.9 eV) [29,30]. Ga₂O₃ is a promising candidate for power devices and optoelectronics [31-34], visible-blind UV-light sensors [28], memory devices [33] and gas sensors [35]. These applications can be downscaled to the nanoscale, including flexible nanodevices, aligning with the current trend in electronic technologies emphasizing the development of adaptable electronic devices [36,37]. Consequently, understanding the mechanical properties of β -Ga₂O₃ NWs becomes crucial. However, minimal research has been dedicated to exploring and understanding the mechanical properties of β -Ga₂O₃ NWs [38].

Metal oxide NWs like copper oxide (CuO), known for their high optical absorption coefficient and the lowest band gap energy among metal oxides, hold promise as materials for visible light photodetectors, offering transparency and flexibility. The optoelectrical properties of CuO, such as its bandgap range and surface depletion layer for charge capturing, can be tailored for specific applications due to the ease of nanofabrication of the material. This makes CuO NWs suitable for a wide range of uses, including multispectral detection and molecular/thermal imaging. Additionally, the inherent chemical and mechanical stability, along with cost-effectiveness, make CuO a reliable choice for industrial applications [39].

P-type CuO NWs are widely acknowledged as catalysts and have attracted significant interest for various applications, including sensors and nanoelectronics [40]. Studies have revealed that mechanical properties of CuO NWs have been found to be predominantly elastic up to a critical strain, beyond which they undergo brittle fracture [41,42]. Moreover, unique mechanical behaviours, such as anelasticity observed in axially twinned CuO NWs during TEM bending tests, are attributed to the cooperative motion of atoms associated

with twinning [43]. However, no previous research has explored plastic deformation through mechanical manipulation of initially straight, thermally grown CuO NWs post-synthesis. This represents a new area of study, highlighting the potential for discovering additional unique mechanical behaviours in CuO NWs.

Metal nanostructures, such as Ag and Au, including NWs, are a topic of intense interest. Surface plasmons, or collective electronic oscillations, are the primary optical property of these noble metal nanostructures [44]. Au NWs stand out among various materials due to their easy synthesis, precise geometry, and outstanding electrical, optical, and chemical properties. They are employed in numerous applications, including biosensors, catalysts, gas sensors, mechanical energy storage and release, flexible electrodes, and SERS [45].

One of the applications of noble metal NWs in plasmonics, is in the fabrication of substrates for SERS. It is an ultrasensitive detection method, capable of providing fingerprint information of small molecules and even single molecule detection [46]. When compared to regular Raman signals, SERS significantly boosts Raman signals by a factor of up to 10^{14} . Due to this remarkable enhancement caused by the strong light-induced electric field at certain regions within the metallic nanostructured space, sometimes referred to as "hot spots", SERS is an appealing high-sensitivity and selectivity detection technique for the target analytes [47]. Numerous nanofabrication techniques have been utilized to create highly ordered SERS substrates, including electron beam lithography, electro-oxidation lithography, UV photolithography, nanoimprint lithography, and self-assembly [28]. However, exploring alternative methods to utilize metal NWs and their thermal behaviour could offer new opportunities for creating cost-effective SERS substrates.

Metal NWs also offer both electrical conductivity and sufficient transparency when arranged on a transparent substrate in the form of a low-density mesh. The growing demand for transparent conductive materials has prompted extensive research efforts focused on the design, synthesis, and characterization of such materials [48,49]. Among the various materials investigated for NW-based transparent electrodes, Ag NWs stand out as one of the most extensively studied due to their ability to be synthesized in large quantities with precise control over their length and diameter [50,51]. Ag NW networks find application in highly flexible transparent film heaters [52] and have also attracted interest as a fundamental component in neuromorphic computing devices in recent years [53]. In the context of the applications above, Ag NWs experience increased temperatures due to Joule heating [54]. Besides, elevated temperatures can lead to the fragmentation of NWs into shorter segments, often explained by Rayleigh instability and energy minimization

through spheroidization [55,56]. A deeper understanding of the heat-induced behaviour of Ag NWs under different conditions and on various substrates could enhance control over cost-effective production methods for novel applications involving arrays of metal nanostructures.

2.3. Structure

The structure of a material, which is the arrangement of its internal components, is crucial in determining its properties, potential applications, and performance [57]. Materials can exhibit various types of translational symmetry, influencing their structural complexity and typical properties such as mechanical, optical, magnetic, and electronic behaviours [58]. Single crystals have a perfectly periodic arrangement of atoms throughout the specimen, forming a continuous and uniform structure. Moreover, these crystals can be naturally occurring or artificially grown under controlled conditions, often taking on regular geometric shapes with flat faces. Single crystals are essential in modern technologies, particularly in semiconductor applications like silicon microcircuits [59]. However, defects within crystalline structures, such as point, linear, and planar defects, significantly impact material properties. Point defects like vacancies and interstitials affect mechanical properties, while dislocations and planar defects disrupt atomic arrangement, influencing material behaviour [59-63].

NWs often exhibit specific types of defects, such as kinks, which are abrupt changes in growth direction and are usually associated with twin boundaries. These defects commonly occur during synthesis methods involving metal catalyst nanoparticles, like chemical vapor deposition and molecular beam epitaxy [23,64,65]. The growth direction of NWs is influenced by factors like surface free energy, pressure, temperature, and reactor atmosphere composition, leading to uniform or altered crystallographic orientations [65]. Defects like dopants, oxygen vacancies, nano-twins, and kinks can modify the properties and functionalities of NWs. Kinked NWs, in particular, are of interest for their potential applications in electronic and nanomechanical devices due to their mechanical durability. Moreover, advanced synthesis techniques allow for substantial control over kink occurrence by adjusting growth parameters [66].

While defects can degrade the fundamental characteristics of NWs, straight and defect-free NWs are preferred for most applications. However, kinks can also provide additional means of property control and introduce novel characteristics, making them valuable in integrated electronic devices, nanoelectronic bioprobes, and nanoscale springs [23,67]. In contrast, metal NWs commonly exhibit a reversible cyclic deformation mechanism involving twinning and detwinning under tensile and compressive loading, respectively,

which can occur post-synthesis and accommodates large strains, enabling ultrahigh strength and ductility [68,69].

The closest experiments related to the kinking of non-metallic NWs include recent findings in structural defects and mechanical behaviour of nanoscale covalent materials, which have revealed unique and fascinating mechanical properties not observed in their bulk forms [70]. For instance, Östlund et al. [71] discovered the ductility of micromachined Si pillars comparable to that of metals in compression tests at room temperature, with Si sample sizes reduced below 300 nm. Similarly, Wu et al. [72] reported a transition from brittleness to plasticity during compressive deformation at room temperature in monoclinic β -Ga₂O₃ single crystals, with pillar sizes reduced below 800 nm. The crystallographic orientation of the micropillars was found to be crucial for observing plasticity at small scales. Additionally, Mignerot et al. [73] observed plastic deformation of InSb micro-sized pillars during micro-compression tests at room temperature, leading to stress-induced nano-twin formation. To further reduce specimen size, a convenient alternative is the direct synthesis of nanostructures, particularly NWs.

2.4. Mechanical properties

As particle sizes reach atomic dimensions, the physical and chemical properties of materials can undergo significant changes. These changes are influenced by quantum mechanics and surface phenomena, as the proportion of atoms on surface sites increases with decreasing particle size [59]. Mechanical properties describe how materials respond to external stresses and conditions. Conventional materials exhibit properties such as strength, brittleness, plasticity, toughness, hardness, elasticity, fatigue strength, rigidity, ductility, and yield stress. Non-metallic inorganic materials are typically brittle, lacking elasticity, toughness, ductility, and plasticity, while certain organic materials are flexible [74].

Nanomaterials are used in various applications, including flexible nanodevices and nanoelectromechanical systems (NEMS). Thus, understanding the mechanical properties of NWs, such as the elastic modulus, is vital for designing nanomechanical resonators and flexible field-effect transistors [36,37,75,76]. Research efforts aim to improve the mechanical properties of nanomaterials, including impact resistance, fracture, bending strength, Young's modulus, and tensile strength. This requires examining factors like surface structure, functionalization, fabrication techniques, and chemical treatments, as well as the material composition and its defects [74,75].

Over the past decades, various methods have been developed to analyze the mechanical properties of NWs. These methods include direct measurements

such as bending, uniaxial loading, and indentation, as well as indirect approaches like vibration. However, manipulation of NWs for testing poses significant challenges due to their small size [6]. The elastic properties of NWs can be assessed using conventional techniques for 1D nanostructures, including tensile tests, resonance methods, cantilevered beam bending, three-point bending, nanoindentation, buckling, and contact resonance AFM [77]. AFM is particularly valuable for measuring the force-displacement response with high resolution. Furthermore, techniques like AFM three-point bending are widely used to determine the Young's modulus of NWs by securing a NW across a trench and applying force to its midpoint with an AFM tip, measuring the resulting deflection [78-80]. Incorporating AFM, nanoindenter, nanomanipulator, or microelectromechanical system (MEMS) devices into electron microscopes allows real-time observation of atomic-scale deformation of NWs under load. These in situ techniques provide powerful insights into the mechanical properties of NWs during testing, enhancing our understanding of their behaviour under various conditions [6].

2.4.1. Elasticity

The mechanical behaviour of a material under external force or load can be evaluated through stress-strain tests. If the load is constant or changes gradually and is evenly distributed, the material's response can be measured. These tests are conducted in three primary modes: tension, compression, or shear. In tension tests, a specimen is deformed until fracture by applying a uniaxial tensile load. Compression tests are similar but use compressive force, causing contraction. Shear tests apply forces parallel to the surface, causing layers to slide past each other. Torsion occurs when forces cause an object to twist about its longitudinal axis [59].

Understanding the elastic behaviour of nanostructures is crucial for both applications and insights into their synthesis. Techniques like AFM three-point bending tests, nanoindentation, and *in situ* methods are used to study the mechanical behaviour of NWs. These techniques enable real-time monitoring and measurement of elastic parameters such as hardness and Young's modulus, as well as exploring NWs' plasticity [81,82]. However, characterizing NWs' mechanical properties is challenging due to the precision required at the nanoscale. Accurate measurement of Young's moduli is necessary as NWs may exhibit size-dependent behaviour due to defects and surface stress [8]. Indirect techniques, like SEM and AFM nanomanipulations, provide valuable insights by measuring force-displacement behaviour during manipulation to estimate elastic modulus.

2.4.2. Adhesion

Adhesion involves the molecular interactions at material interfaces, specifically between an adherend and an adhesive, forming an adhesive joint. This joint comprises multiple interfaces, adding complexity to its structure [83]. Furthermore, adhesion is crucial for nanostructures, especially for the adherence of NWs to substrates post optical or laser processing, vital for device fabrication [82]. Furthermore, adhesion and static friction of metal nanostructures decrease notably after annealing due to contact area reduction with the substrate. AFM manipulation techniques effectively assess adhesion and static friction, estimating the portion of movable NPs. This is essential for methods like heat-induced NW fragmentation for creating SERS substrates [84].

Adhesion is also vital in flexible electronics, ensuring components remain reliable and intact. Flexible electronics, including artificial e-skin, flexible touch sensors, health monitoring systems, and implantable devices, maintain electrical performance under mechanical stress [5,85]. Thus, experimental setups for evaluating nanomaterial adhesion and mechanical properties often use AFM. A hard, spherical probe applies controlled pressure onto a sample, measuring interaction force and probe displacement. Indentation curves reveal mechanical properties, while the pull-off force during retraction indicates adhesion strength. The attractive force during approach is lower than the pull-off force, attributed to non-adiabatic experimental conditions [86].

2.5. Thermal properties

Thermal properties, such as thermal expansion and heat capacity, describe how materials respond to temperature changes [59]. Moreover, the thermal behaviour of metal nanostructures at elevated temperatures differs significantly from their bulk counterparts, depending on material, size, and shape [87,88]. The melting point of nanostructures decreases as their size reduces, often reaching much lower temperatures compared to bulk materials [89]. This is particularly important for applications where NWs are exposed to high temperatures or require thermal treatment to remove organic residues. Heatinduced fragmentation can hinder functionality, especially in NW-based transparent conductive coatings [90].

Furthermore, networks of Au and Ag NWs can spheroidize when heated due to Rayleigh instability, which causes the NWs to fragment into NPs to minimize surface area through surface tension. This phenomenon, observed in both fluids and specific metallic nanostructures, has been extended to solid NW systems and explains morphological changes driven by surface curvature [9,10].

Studies have confirmed this model by annealing Cu NWs on Si substrates, aligning with predictions of the beading phenomenon [91].

Recent studies investigating the thermal behaviour of Au NPs, have revealed that when subjected to annealing experiments at progressively higher temperatures, these NPs undergo a notable transformation in shape, transitioning from irregular faceted shapes to more rounded ones. This phenomenon is believed to occur due to a process driven by diffusion, aiming to minimize the surface energy of the particles. Additionally, experiments using AFM to manipulate these particles have shown that higher annealing temperatures generally lead to increased particle mobility [92]. However, this could pose a significant challenge to the long-term reliability of NW-based components, prompting the exploration of various methods to mitigate Rayleigh instability. Conversely, if the morphological changes driven by instability can be controlled, they could offer a promising nano-patterning approach [93].

3. EXPERIMENTAL TECHNIQUES

3.1. Microscopy techniques

3.1.1. Scanning electron microscopy

The resolution of optical microscopy is limited by the wavelength of light, which is on the order of hundreds of nanometers, even in the ultraviolet range. As an alternative, electron beams have been used to examine structural details at much smaller scales [94].

Moreover, electron microscopy uses focused accelerated electrons to examine samples at a very small scale, achieving higher magnification and superior resolution [95]. When the electron beam interacts with a specimen, it reveals critical details about the specimen's composition, crystalline structure, feature size and shape, and surface characteristics [96]. An SEM uses a focused electron beam to scan a surface, creating images from the interaction signals of the sample's atoms and electrons. An image forms by combining signal intensity with the beam's position in a raster pattern [97,98].

3.1.2. Transmission electron microscopy

Transmission electron microscopy (TEM) creates images by passing an electron beam through an ultrathin sample, typically less than 100 nm thick, or a suspension on a grid. This process generates images and electron-diffraction patterns, useful for studying crystalline materials. TEM uses an electron gun and multiple magnetic lenses to focus the electron beam onto the specimen, affecting the image's intensity and resolution. The specimen stage allows for precise positioning, with mechanical stability crucial for high spatial resolution. The imaging system, consisting of at least three lenses, produces a magnified image or diffraction pattern on a fluorescent screen or electronic camera. The lens design and operation impact the image's magnification and resolution [99,100].

Electron beams can be diffracted by atomic planes in the sample, creating diffraction patterns. For crystalline samples, these patterns appear as rings for polycrystalline or amorphous materials, or dots for single crystals, revealing the crystal's orientation and space group symmetries [100].

3.1.3. Atomic force microscopy

AFM is a type of scanning probe microscopy that uses a sharp probe scanned across a surface to produce high-resolution images, potentially at the sub-nanometer scale. The AFM probe, a stylus that interacts directly with the surface, maps out the repulsive and attractive forces between the probe and the

sample, creating a high-resolution three-dimensional topographic image of the surface [101]. Figure 3.1(a) shows the relationship between the force exerted between the tip and the sample and the distance separating them.

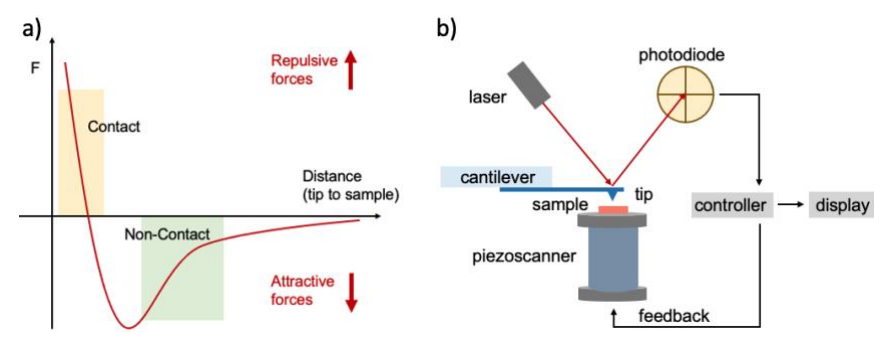


Figure 3.1. (a) Dependence of the force between tip and the sample on distance between them. Adapted from [102]; (b) AFM operation principle. Adapted from [103].

AFM employs a sharp-tipped, micrometre-scale cantilever to scan a sample at nanometer distances, detecting interatomic forces. A laser and photodetector measure cantilever deflection, and the interaction force varies nonlinearly with tip-sample separation. In contact mode, the tip remains in the repulsive zone, maintaining consistent force but causing tip wear and potential sample damage. Non-contact mode involves the tip oscillating above the sample, while tapping mode entails brief tip-sample contact during each oscillation. Cantilevers, typically V-shaped or rectangular, are made of silicon or silicon nitride, with a reflective surface for laser detection. The probe's sharpness or attached spherical particles determines its application, whether for high-resolution topography or adhesion measurements [86,104]. The basic set-up of a typical AFM is shown in *Figure 3.1(b)* [103].

3.2. Nanomanipulations

A micro/nanomanipulation and assembly techniques are essential for applications ranging from the micrometer to the nanometer scale. Over the past decade, these techniques have been widely used in fields such as micro/nanostructure assembly and material characterization [105]. Nanoscale manipulation experiments serve two main purposes: exploring material properties like friction and mechanics at the nanoscale, and enabling precise 2D positioning and assembly of nanostructures. These capabilities are crucial for

applications in nanoelectronics, NEMS, and digital information storage [106]. Manipulations can be performed in both electron microscopes and AFM setups.

Micromanipulation involves either transporting pre-existing objects for investigation or assembling complex structures from basic components. In electron microscopes, micromanipulation allows handling individual micro- and nanoobjects with nanometer precision, with the process and results visible in high resolution and real-time [107].

3.2.1. Stepper motors and piezoelectric actuators

Manipulator drives use stepper motors, which move in response to electrical pulses and can position without feedback sensors. However, they have limitations such as vibration, resonance, limited dynamics, locking torque, high temperatures, reduced efficiency, and lower positioning accuracy [108]. In real-world conditions, without a position sensor, the rotor's actual position may deviate from the preset due to step skipping [109].

In recent years, companies like Physik Instrumente, NanoControl, and Nanomotion have developed piezoelectric-based actuators for precise positioning at the micrometer and nanometer scale. The Kleindiek MM3A-EM shown in *Figure 3.2*, is a notable commercial manipulator using piezoelectric stick-slip actuators. A significant challenge in micromanipulation is controlling these actuators due to their discrete step nature. Additionally, the step sizes of these actuators are variable, depending on factors like external loads, the mass of the manipulator's links, and environmental conditions. Moreover, these devices often lack sensor feedback, making closed-loop control difficult [110].

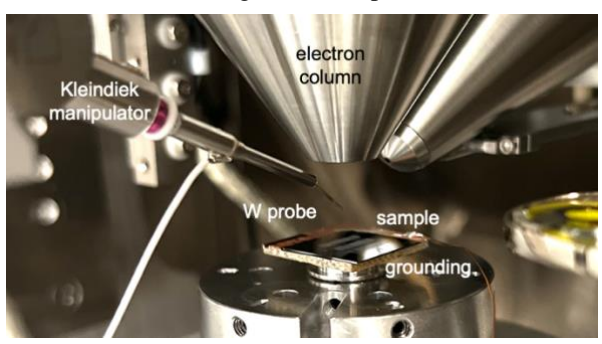


Figure 3.2. The Kleindiek MM3A-EM micromanipulator in SEM Tescan Lyra chamber.

4. MATERIALS AND METHODS

4.1. CuO nanowire synthesis and characterisation

CuO NWs were grown by annealing a copper foil at 400° C for 2h at ambient atmosphere. Thermal treatment was carried out in a tube furnace [66]. The initial morphological analysis of the as-grown CuO NWs on the original substrate was performed inside SEM Helios NanoLab 600. The NWs were straight, with lengths of 5 to 10 μ m and diameters of 50 to 200 nm.

SiO₂/Si(100) wafers (Semiconductor Wafer, Inc.) with 50 nm thermal oxide were used as substrates for conducting further experiments with individual NWs. Using standard Si micromachining methods, micropatterned Si substrates featuring regular rows of pyramidal holes were fabricated. The resulting cavities were ideal for conducting mechanical tests on suspended NWs [45].

Partially suspended CuO NWs were mechanically manipulated on sample substrate by pushing the suspended end of the NW with a sharp tungsten probe attached to a micromanipulator Kleindiek MM3A-EM. Experiments were conducted inside SEM Tescan Lyra XM.

4.2. Ga₂O₃ nanowire synthesis and characterisation

 Ga_2O_3 NWs were synthesized using atmospheric pressure chemical vapor transport in a horizontal quartz tube reactor via the VLS mechanism. Ga_2O_3 NWs up to $100~\mu m$ long were grown at $850\text{-}900^{\circ}\text{C}$.

TEM (Tecnai GF20, FEI) at an accelerating voltage of 200 kV provided information on the crystalline structure of the NWs. Fast Fourier transformation (FFT) was performed on the obtained TEM images to determine crystalline orientations. The structure was also analyzed using X-ray diffraction (XRD) on Rigaku MiniFlex 600 X-ray powder diffractometer. The morphology of asgrown NWs was examined using SEM Helios 5 UX DualBeam. The measurements were performed at an acceleration voltage of 5 keV and a beam current of 25 pA.

The synthesized NWs were mechanically placed onto the etched patterned Si wafers. Schematics of Si substrates used for mechanical resonance and three-point bending tests are shown in *Figure 4.1*. Resonance measurements were conducted employing a Kleindiek MM3A-EM micromanipulator equipped with a finely pointed tungsten probe. Resonance within the NWs for *in situ* SEM resonance measurements was induced by applying a sinusoidal AC signal between the NW and the tungsten probe, serving as the electrode. The excitation signal was generated by a waveform generator (RIGOL DG4162).

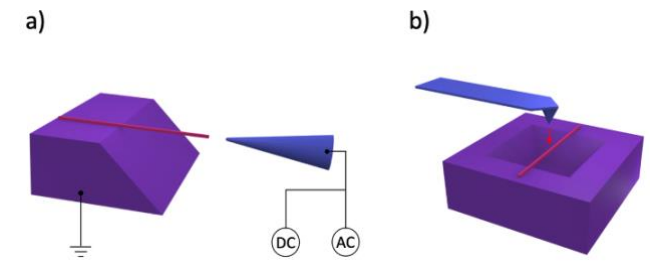


Figure 4.1. Schematics of Si substrates used for mechanical resonance and three-point bending tests: (a) NW suspended above the etched trench with one end immobilized and a tungsten needle applying potential for resonance measurements in SEM; (b) NW suspended over the inverted pyramid with both ends secured for three-point bending measurements in AFM.

Elastic modulus was determined from the observed resonance frequencies as follows [111]:

$$E_{res} = \frac{48\pi^2 \rho}{\beta_n^4} \frac{L^4}{W^2} f_n^2, \tag{4.1}$$

where E_{res} is the elastic modulus, β_i is a constant for the i-th harmonic (for the first harmonic (i=1), $\beta_l \approx 1.875$), W is the width of the NW, ρ is the density of the bulk material, v is the NW resonance frequency, and L is the length of the NW.

The Young's modulus of a NW was calculated using the three-point beam bending theory for a beam with two fixed endpoints in the following way [78]:

$$E_{tpb} = \frac{F \cdot L^3}{192 \cdot \delta \cdot I'},\tag{4.2}$$

where F is the applied force, L is the suspended length, δ is the displacement of the NW and I is the second area moment of inertia [112]. The second area moment of inertia for a rectangular beam is given by:

$$I = \frac{w \cdot h^3}{12},\tag{4.3}$$

where w is the width of the NW and h is the height of the NW.

4.3. Au nanowire synthesis and characterisation

Au nanostructures were synthesized by solution-based seed mediated growth. The synthesized NWs were a few μm long with a diameter of

approximately 50 nm [99]. SEM studies were performed using the Helios 5 UX DualBeam with an acceleration voltage of 5 keV and a beam current of 25 pA.

Manipulation of NPs was conducted using an AFM Dimension Edge Bruker equipped with a rectangular AFM cantilever (NCHR, Bruker) characterized by a force constant of k=42 and a resonance frequency of 320 kHz. The formula developed by Anczykowski et al. [113] was used to calculate the dissipated power:

$$P = k \cdot f_0 \cdot (A_{set} \cdot A_{piezo} \cdot sin\theta - A_{set}^2 / Q), \tag{4.4}$$

where k is the cantilever's force constant, f_0 is the cantilever's resonance frequency, A_{set} is the setpoint amplitude, A_{piezo} is the driving amplitude, θ is the phase signal, and Q is the quality factor of the AFM cantilever. The phase signal was extracted from tapping mode phase images using the Gwyddion software (version 2.63) [84].

Raman spectroscopy was conducted using the Princeton Instruments TriVista CRS Confocal Raman Microscope (TR777), equipped with three monochromators and a microscope featuring diffraction gratings with line densities of 600, 900, and 1800 lines/mm, and a focal length of 750 mm. The enhancement factors (EFs) for Rhodamine B molecules were calculated according to the equation [84]:

$$EF = \frac{I_{SERS}/C_{SERS}}{I_{RS}/C_{RS}},\tag{4.5}$$

where I_{SERS} is the Raman intensity and C_{SERS} is the concentration of Rhodamine B used in SERS measurements; I_{RS} is the Raman intensity and C_{RS} is the concentration of Rhodamine B used in routine Raman measurements.

4.4. Ag nanowire characterization

Ag NWs measuring approximately 120 nm in diameter and tens of μm in length were procured from Blue Nano, Inc. These NWs exhibit a pentagonal cross-section and an inner structure characterized by five-fold twinning [114]. A distinct set of experiments was conducted on Ag NWs within a TEM to investigate the impact of heat treatment on the internal structure of the NWs. For the heating experiments, Cu TEM grids with a 20 nm Al₂O₃ layer applied via atomic layer deposition were used. Two TEMs, Tecnai GF20 by FEI and the JEOL model ARM-200F, were utilized, operating at an accelerating voltage of 200 kV.

5. RESULTS AND DISCUSSION

5.1. Post-synthesis kinking in CuO nanowires

The properties and functionalities of NWs can be altered by introducing different defects, such as nano-twins [115,116] and kinks [117]. Kinked NWs are gaining interest for their potential applications in electronics [117-119] and nanomechanical devices [120,121], as well as for their reported enhancement in mechanical durability [122].

In this section, three different manipulation scenarios leading to post-synthesis kinking are described in detail. Furthermore, the experiments demonstrate the possibility of reversible plasticity in CuO NWs, as evidenced by the complete unkinking of a single NW in one instance. Molecular dynamics (MD) simulations support the experimental findings and elucidate a mechanism of reversible deformation-induced crystal twinning. The findings presented in this section have been published in **Paper I**.

5.1.1. CuO nanowire transfer onto substrates

The NWs were mechanically transferred onto three distinct types of Si substrates through manual manipulation. This process involved pressing and then shearing the Cu foil, along with the attached NWs, against the substrates, as illustrated in *Figure 5.1*. Type I substrates consisted of unetched Si wafers, where the NWs lay flat on the surface. Type II substrates featured square-shaped etch pits with dimensions on the order of a few micrometers in length and the depth in the range of several hundreds of nanometers.

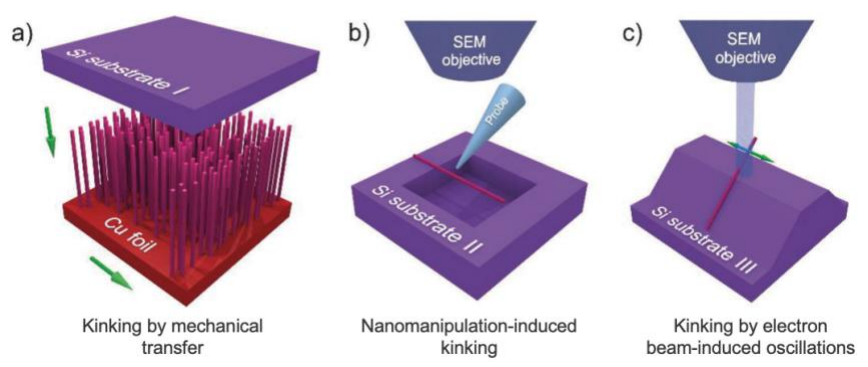


Figure 5.1. Schematic representation of the sample substrates, the positioning of the CuO NWs on them, and the manipulation operations that induced kinking.

Lastly, type III substrates comprised parallel trenches with a width of 3 μ m, separated by planes of unetched Si measuring 900 nm wide. The sidewalls of the pits and trenches had a slope relative to the main surface of Si at an angle of 54.7 degrees, corresponding to the angle between the (111) and (001) planes in Si wafer. Consequently, some NWs were partially exposed above the etch pits and trenches on the type II and III Si substrates.

5.1.2. Kinking by mechanical transfer

Upon examining the CuO NWs that underwent mechanical transfer onto the Si sample substrates or the Si TEM grid, as illustrated in Figure 5.2(a), it was noted that a considerable portion exhibited deformations resembling "kinks". These deformations entailed an abrupt change in orientation while maintaining their structural integrity. Notably, no kinked NWs were observed on the original growth substrate, suggesting that this transformation occurred during the mechanical transfer process. The kinking angles of the CuO NWs appeared to fall within a very narrow range, as depicted in the inset of Figure 5.2(a), with a median value of 143.2 ± 2.9 degrees. This measurement was derived from the analysis of SEM images of fifty kinked NWs on the type I (flat) sample substrate, as shown in Figure 5.1(a). The uniformity of these angles implies a direct correlation between the observed deformation and the structure of the CuO crystal, rather than being a random defect. Furthermore, with few exceptions, which could likely be attributed to post-kinking fracture, the kinked NWs consistently exhibited a double kink that divided the NW into three segments, as depicted in Figure 5.2(a). Additionally, in most cases, NWs with multiple double kinks were observed.

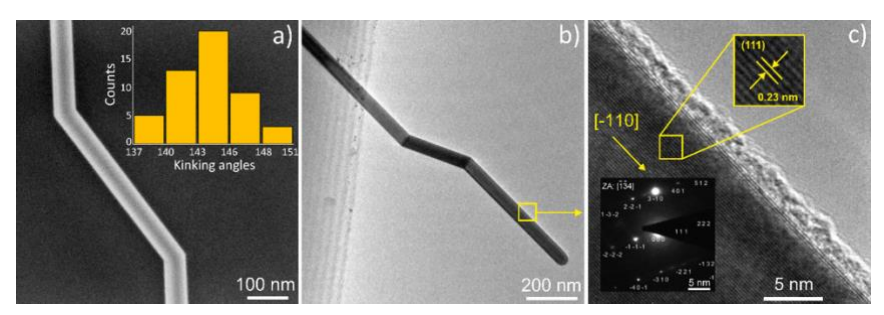


Figure 5.2. (a) SEM micrograph of a CuO NW kinked after mechanical transfer on a flat Si substrate. The inset presents a histogram displaying the distribution of kinking angles; (b) TEM image capturing a CuO NW with kinks; (c) TEM image of the same NW at higher magnification alongside its corresponding

selected area electron diffraction (SAED) pattern. The arrow denotes the growth direction of the NW, which is $[\bar{1}10]$.

5.1.3. Nanomanipulation-induced kinking and unkinking

A series of nanomanipulation tests were conducted on partially suspended CuO NWs transferred onto a structured Si wafer (Substrate type II) to investigate their response to external mechanical loading. A tungsten probe attached to a nanomanipulator was used to push the NWs (see *Figure 5.1(b)*). The experiments were carried out within SEM, allowing real-time visual feedback. The movement of the nanomanipulator occurred either smoothly within the "scan mode" of the piezo scanner, with a limited range of a few microns, or abruptly within the "step mode", based on the stick-slip motion of the piezoelectric actuator. This abrupt movement induced fast-decaying oscillations in the manipulator-probe system. It was observed that abrupt movement of the probe could cause kinking in CuO NWs protruding over the etch pit of the Si substrate sample. However, the timescale of kinking events was below the temporal resolution of the SEM scanning rate, allowing only pre- and post-event image observation.

Figure 5.3(a-e) depicts the sequence of mechanical nanomanipulations aimed at inducing kinking in a single CuO NW. The CuO NW is partially suspended over the etch pit of the Si sample substrate (the darker area represents the bottom of the pit). Initially, the nanomanipulator probe is positioned near the NW, and then it pushes the NW against the sidewalls of the pit. At a certain point (see Figure 5.3(c)), the manipulator executes an abrupt movement ("step"), resulting in the kinking of the NW. In most cases where kinking was achieved, the kinked region was near the sharp edge or corner of the pit. Twenty-three kinking events were recorded during nanomanipulation experiments, although brittle fracture of NWs was a more common outcome of manipulation in "step mode".

No kinking was observed during manipulation in scan mode, indicating specific conditions are needed for mechanically induced kinking. Kinked NWs exhibited durability and elastic behaviour when pushed, maintaining the angle even without external force. Severe deformations or abrupt movements may cause breakage at the kink, but fractures typically occur randomly outside the kinked region, suggesting no significant weakening at the kink. Selected frames from a single nanomanipulation experiment performed on a previously kinked CuO NW are illustrated in *Figure 5.3(f-h)*. The probe of the nanomanipulator maneuvers beneath the CuO NW and then gradually shifts it sideways and upward. Upon retraction of the probe, the NW promptly restores its original shape without experiencing any additional deformation, thereby preserving both the kink location and kinking angles.

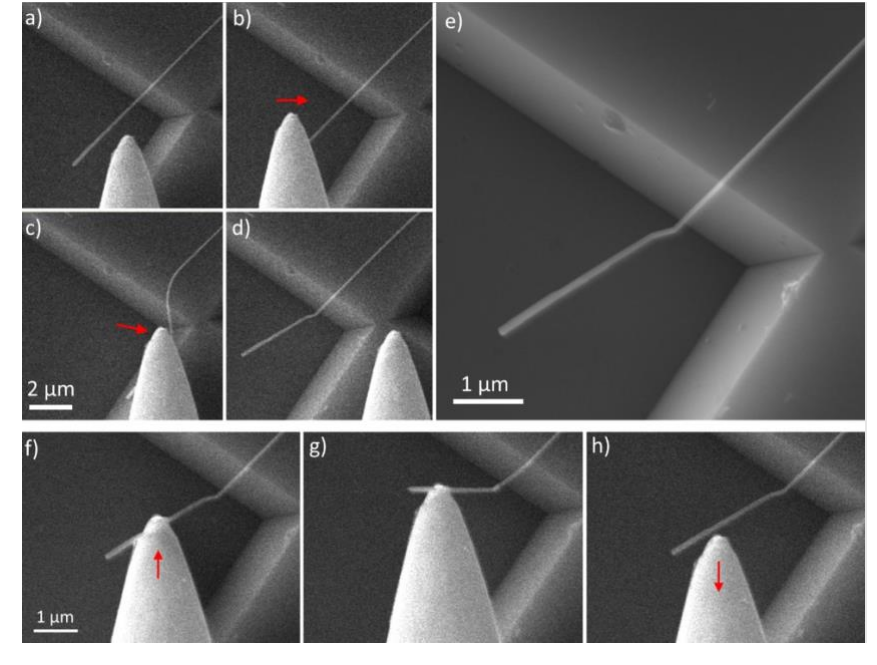


Figure 5.3. Kinking induced by nanomanipulation in a CuO NW.

In a single instance, a CuO NW was successfully kinked and subsequently straightened back to its initial profile (see *Figure 5.4*). The probe was positioned closely above the NW and then moved using a coarse nanomanipulator motion (see *Figure 5.4(b)*). As the probe was retracted, the NW appeared to be kinked (see *Figure 5.4(c,d)*). Subsequently, the kinked NW was pushed and displaced by the probe (see *Figure 5.4(e,f)*) to assess if it would break at the kink. Unexpectedly, upon retracting the probe, the NW appeared not only intact but also straightened (see *Figure 5.4(g,h)*). This reversal of the kinking process appears to necessitate even more specific conditions compared to the initial kinking, as similar outcomes were not achieved with other NWs. It appears that a crucial factor is the suspension of a sufficiently long NW over the pit, maintaining its suspended state.

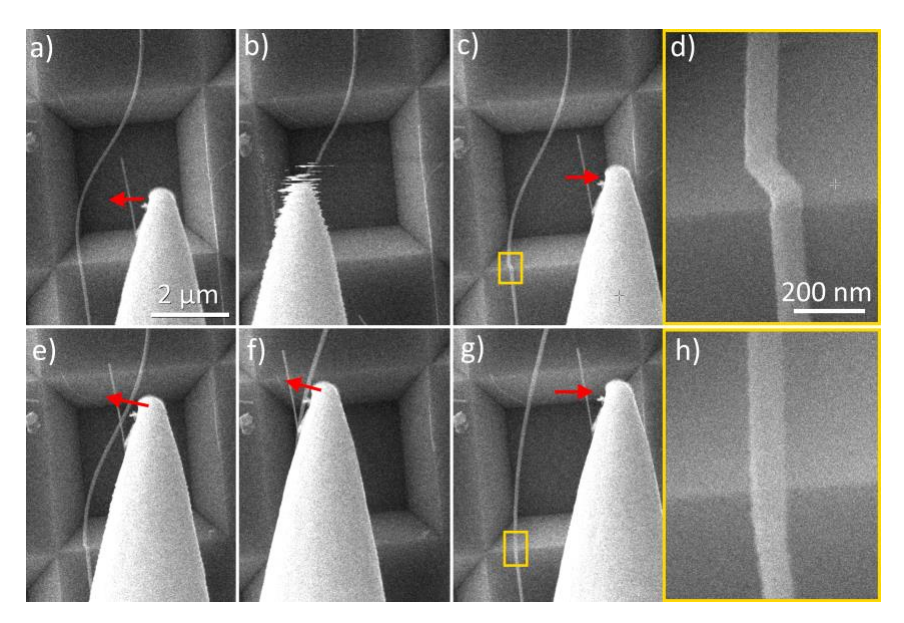


Figure 5.4. The manipulation of a single CuO NW to induce both kinking and subsequent unkinking.

5.1.4. Electron-beam-induced oscillation followed by kinking

It was observed that kinking of CuO NWs can also be achieved through electron-beam induced oscillations of the free-standing portion of a NW. This phenomenon was noted for NWs transferred onto the type-III patterned Si sample substrate (see Figure 5.1(c)). It occurred at a slow e-beam scanning speed, inducing auto-oscillations in the protruding part of the NW. An instance of this is illustrated in *Figure 5.5*. Initially, to sacrifice image quality, the NW is imaged at a high scan rate (few frames per second) to prevent the electron flux from inducing oscillations (see Figure 5.5(a)). Subsequently, the NW is imaged at a slower scanning speed, leading to self-oscillations in the NW. These oscillations are noticeable by the smeared appearance of the NW part above the red arrow in Figure 5.5(b), as SEM imaging progresses line by line (horizontally) from the top left corner to the bottom right corner. When the beam reaches the position marked by the red arrow in Figure 5.5(b), the oscillating segment makes contact with the substrate. Consequently, Figure 5.5(b) displays partial data from two states of the NW in a single image. The upper portion above the red arrow corresponds to an oscillating NW, while the lower part depicts the NW resting against the top plane of the Si structure. By this juncture, a kinking event has

already occurred. The outcome of the oscillation-induced kinking is illustrated at various magnifications in Figure 5.5(c,d).

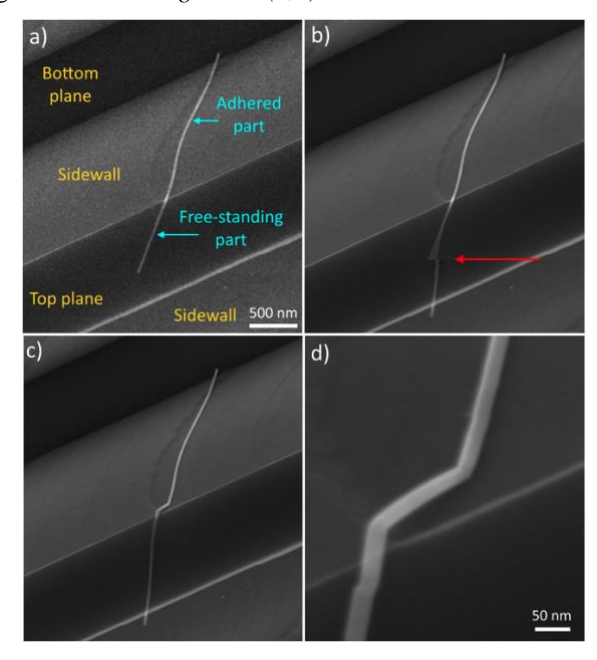


Figure 5.5. Oscillation induced by electron beam, subsequently resulting in kinking of the CuO NW situated on the structured Si substrate. The accelerating voltage of the electron beam is 10 kV.

5.1.5. Structural characterization of the kinked CuO nanowires

In order to understand the kinking mechanism, a detailed examination of the exact crystallographic structure of the NWs at the kink area was needed. To accomplish this, CuO NWs were mechanically transferred on Si TEM grids and high-resolution TEM imaging was conducted on several kinked CuO NWs that were kinked by the transfer. $Figure\ 5.6(a)$ presents a TEM image depicting a kinked NW precisely at the kinked area. In $Figure\ 5.6(b)$, a closer examination of the kink is performed to observe its precise crystallographic structure. Additionally, $Figure\ 5.6(c)$ displays the corresponding SAED image of the same kink region.

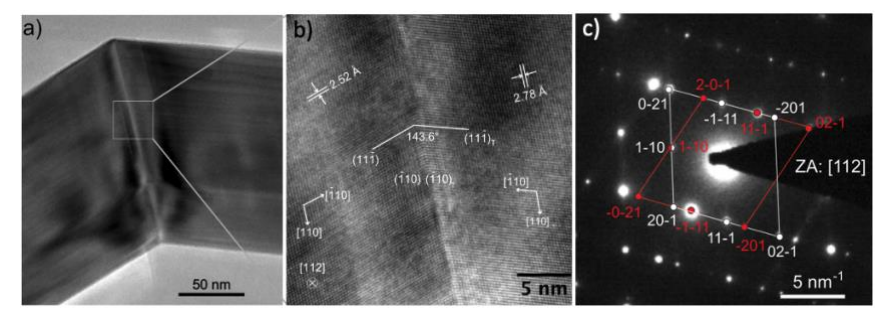


Figure 5.6. (a) TEM micrograph capturing the kinked segment of the CuO NW; (b) High-resolution TEM image of the region specified in (a). (c) SAED image of the identical kink region. The SAED image integrates reflections from both the left and right portions of the NW (before and after kinking), with corresponding sets of reflections indicated by white and red rhombi.

Figure 5.6(b) strongly indicates that the kink is formed by a twin boundary. The deeper investigation of its exact crystallographic structure starts with the hypothesis that the twinning plane is the $(\bar{1}10)$, i.e., parallel to [110], [112], and [001], and the growth direction is $[\bar{1}10]$, as indicated in Figure 5.6(b). Observations reveal that the SAED image exhibits a good alignment with the zone axis, identified as [112]. To precisely assess the crystallographic structural features depicted in the TEM image, an analysis of its periodicities was conducted through two-dimensional Fourier analysis.

The complete kink angle predicted theoretically by the hypothesis, i.e., two times the angle between the direction $[\overline{1}10]$ and the plane $(\overline{1}10)$ is 142.9° , with its projection on the image plane being slightly higher at 143.12° . These values are in excellent agreement with the corresponding value extracted from the Fourier analysis of the TEM image being 143.6° , as well as with the average kinking angle $(143.2^{\circ} \pm 2.9^{\circ})$ found upon measuring many kinked NWs using SEM. Hence, the hypothesis on the crystallographic structure of the kink is confirmed by the experimental data.

5.1.6. Molecular dynamics modelling

In collaboration with Institute of Technology, University of Tartu, a simulation to comprehend the dynamics of the kinking and unkinking process, was conducted on an infinite CuO crystal. This simulation involved introducing a nano-twinned band comprising 4 monoatomic Cu layers, with the twin plane designated as the $(\bar{1}10)$.

Simulations revealed the progression of shear strain and corresponding stress in a Cu crystal. Initially, a positive strain expanded the twinned band by four Cu layers. After relaxation, the system remained in a deformed state with an enlarged twinned band. Applying shear strain in the opposite direction caused the twin planes to contract through a series of plastic deformations, evident as oscillations on the stress curve. Following further atomic rearrangements, the twin band was completely eliminated, resulting in a defect-free crystal. This demonstrates how shear stresses can induce and subsequently eliminate twinned band defects in CuO crystals.

5.1.7. Hypothesis of the observed phenomena

In this study, kinking occurred post-synthesis in initially straight NWs under different experimental conditions: mechanical transfer between substrates, *in situ* electron-beam irradiation, and *in situ* mechanical nanomanipulation. All cases showed plastic deformation with double kinking at approximately 143 degrees. Reproducing nanomanipulation and e-beam induced kinking consistently was challenging due to the coarse motion of the manipulator and the uncontrollable momentum and charge transfer from the beam. In contrast, the mechanical transfer scenario, involving numerous NWs under various loading conditions, frequently resulted in kinking, suggesting the e-beam is not essential.

Common factors include partial suspension of NWs and oscillations before kinking. Smooth nanomanipulation or e-beam without specific substrate conditions did not induce kinking. Molecular dynamics (MD) simulations showed shear loading direction specificity, aligning with the low reproducibility of nanomanipulation and e-beam induced kinking, indicating oscillations play a crucial role. Kinking occurred when NWs contacted the substrate, possibly increasing internal shear loading. Triboheat-related temperature rise during mechanical transfer and oscillations may also contribute.

All three scenarios share a plastic deformation mechanism involving deformation-induced twinning, supported by TEM, SAED, and MD simulations. While typical in metals, reversible plasticity in non-metallic nanomaterials is unusual, suggesting the small size and near defect-free crystal structures of NWs enable higher stresses and strains without fracture.

5.2. Mechanical properties of Ga₂O₃ nanowires

In this section, the elastic modulus of individual β -Ga₂O₃ NWs is investigated through two different techniques: *in situ* SEM resonance and three-point bending in AFM. Additionally, the structural and morphological

characteristics of the synthesized NWs are examined using XRD, TEM and SEM. The findings presented in this section are published in **Paper II**.

5.2.1. Ga_2O_3 nanowires

For structural analysis of the as-grown NW arrays on Si $(100)/\text{SiO}_2$ substrates, XRD measurements were performed. The identified peaks correspond to monoclinic β -Ga₂O₃ (ICDD-PDF #41–1103), as shown in *Figure 5.7(a)*.

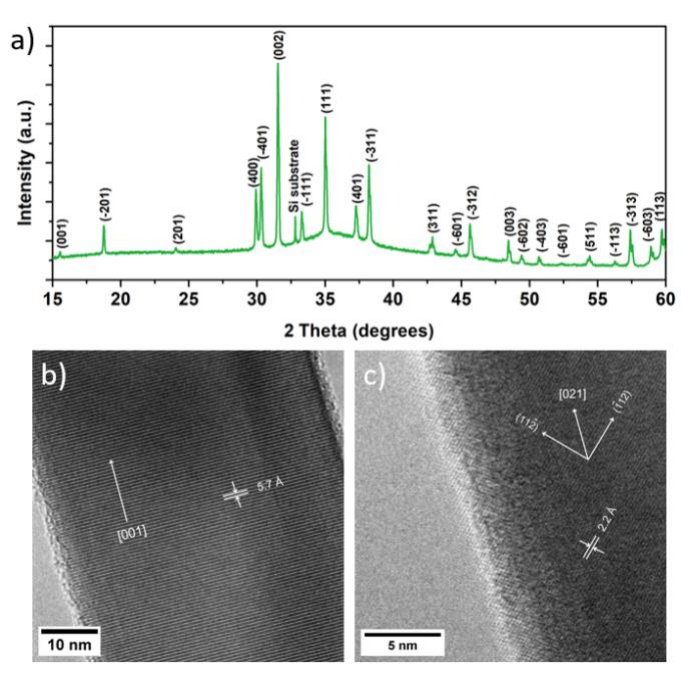


Figure 5.7. (a) X-ray diffraction pattern of β-Ga₂O₃ NWs on Si substrate; (b) TEM image of a β-Ga₂O₃ NW showing an interlayer spacing of 5.7 Å, indicating the [001] growth direction; (c) TEM image of a β-Ga₂O₃ NW showing orthogonal $(11\bar{2})$ & $(\bar{1}12)$ planes with an interlayer spacing of 2.2 Å, indicating the [021] growth direction.

Additionally, the Bragg peak at approximately 33 degrees aligns with the Si substrate (forbidden Si (200) reflection). Furthermore, TEM was employed to examine the inner crystalline structure of individual NWs (refer to Figure 5.17(b,c)). The as-grown NWs typically exhibit single-crystalline characteristics without discernible planar structural defects, such as twin boundaries or stacking

faults. FFT was applied to the TEM images to identify crystalline planes and ascertain the growth direction of the NWs. Multiple NWs were analysed, revealing more than one growth direction, a common occurrence for β -Ga₂O₃ NWs [123]. For instance, *Figure 5.7(b)* illustrates a NW with an interlayer spacing of 5.7 Å, indicating [001] growth direction, while in another NW, as depicted in *Figure 5.7(c)*, orthogonal (11 $\overline{2}$) & ($\overline{1}$ 12) planes were identified, with 2.2 Å interlayer spacing, indicating [021] growth direction. The presence of NWs exhibiting various crystalline orientations suggests either the absence of one dominant preferential growth direction due to the low-symmetry monoclinic phase or the involvement of other growth mechanisms alongside VLS.

5.2.2. *In situ* SEM resonance tests

The mechanical properties of Ga_2O_3 NWs were initially assessed through *in situ* SEM resonance tests. A sequence of SEM images in *Figures 5.8(a-c)* illustrates the excitation of the first mode mechanical resonance in a Ga_2O_3 NW, characterized by a length L = 13.23 μ m and width w = 102 nm, with a resonant frequency f_1 = 126.75 kHz. Under the influence of a 4V AC voltage applied to the probe, the NW demonstrates noticeable oscillations (see *Figure 5.8(b)*).

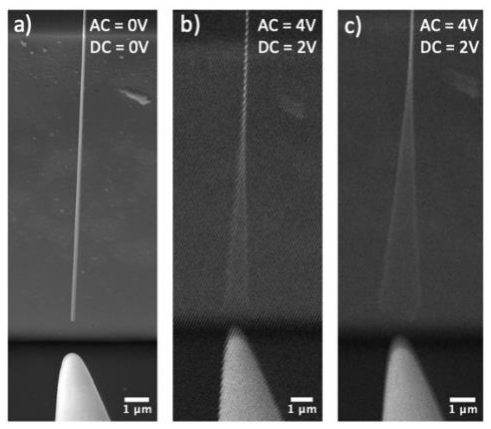


Figure 5.8. SEM images of a NW fixed at one end with a closely positioned probe tip: (a) in the absence of applied AC and DC; (b) showing observable oscillation with 4V AC and 2V DC (non-resonant condition); (c) with 4V AC and 2V DC, demonstrating resonance oscillation.

Upon alignment of the generated frequency with the natural resonance frequency of the NW (see *Figure 5.8(c)*), there is a significant increase in the amplitude of NW oscillations. To ensure the correct identification of the

fundamental natural resonance frequency, oscillations at half of the resonance frequency were examined for each NW, instead of parametric or forced resonance. A total of 26 NWs were measured for their resonance frequency. The width of the NWs varied from 48 nm to 183 nm, while the length ranged from 6 to 27 μ m, and their resonance frequencies varied from 33 to 770 kHz. In the measurements of horizontal (y-axis) resonance oscillations, only the width of the NW was considered for the calculation of the elastic modulus. The mean value of the elastic modulus was determined to be $E_{res} = 34.5$ GPa, significantly smaller than the reported theoretical Young's modulus for the bulk material. No correlation between the measured elastic modulus values and the geometrical dimensions of Ga_2O_3 NWs was observed (see *Figure 5.9(a)*).

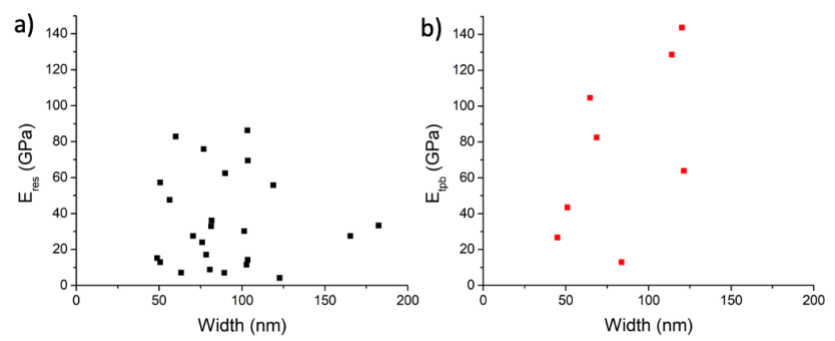


Figure 5.9. Elastic modulus plotted against the width of Ga₂O₃ NWs: (a) derived from SEM resonance examinations; (b) derived from AFM three-point bending experiments. In both cases, widths were determined from SEM images of individual NWs.

5.2.3. Three-point bending tests

The results of the three-point bending tests, as illustrated in Figure 5.9(b), demonstrate considerable data scattering without a discernible dependence on geometric dimensions, mirroring the findings of the resonance technique. The calculated mean value of the elastic modulus stands at $E_{tpb} = 75.8$ GPa, which falls below the elastic modulus observed for bulk Ga_2O_3 . While the dimensions of the NWs used in the three-point bending tests were measured using SEM, the heights were derived from AFM topography data obtained from the adhered sections of the NWs at each end. In Figure 5.10(a), an SEM micrograph depicts the morphology of a Ga_2O_3 NW positioned atop an inverted pyramid structure, with both ends securely fixed to enable controlled three-point bending experiments. Additionally, Figure 5.10(b) presents the AFM topography of the

 Ga_2O_3 NW. Given that the elastic modulus is dependent on the NW height to the third power, measurement errors in height can result in significant scattering. Moreover, certain NWs exhibited non-uniform height distributions, for instance, the height of a specific NW can slightly exceed 20 nm at one end but increase to 80 nm at the other end leading to deviations from beam theory.

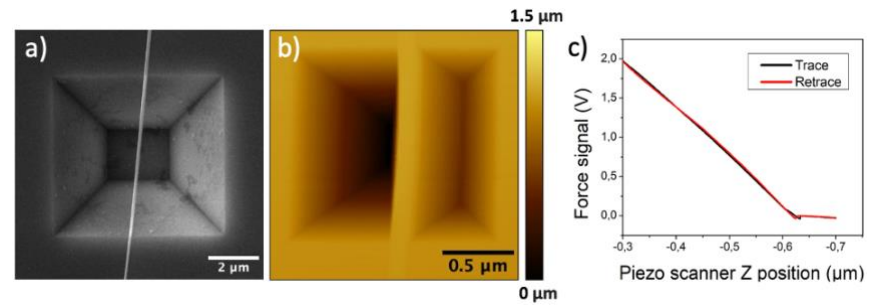


Figure 5.10. (a) SEM image depicting a Ga₂O₃ NW suspended over an inverted pyramid structure with both ends securely fixed; (b) AFM topography image of Ga₂O₃ NW suspended over the inverted pyramid structure with both ends securely fixed, revealing a measured NW height of approximately 23 nm; (c) loading and unloading spectra, illustrating one instance of three-point bending test.

5.2.4. Analysis of the measured elastic modulus values

Observing differences in the elastic properties of Ga_2O_3 NWs compared to bulk material, alongside significant data scatter, raises several potential explanations for this variation. Firstly, both experimental and theoretical investigations have highlighted the substantial anisotropy of β -Ga₂O₃ elastic characteristics, suggesting that Young's modulus strongly depends on the crystalline orientation direction [76,124,125]. This anisotropy, e.g., E_{100} =138 GPa, E_{010} =263 GPa, E_{001} =228 GPa [124], may contribute to the scattering of measured elastic modulus values due to the varied growth directions exhibited by as-grown NWs, as determined through TEM studies.

The elastic modulus of nanostructures depends heavily on their dimensions, leading to scattering effects if these measurements are inaccurate [126]. This issue is complicated by the non-rectangular (e.g., trapezoid) cross-sections of $\beta\text{-}Ga_2O_3$ NWs, requiring thorough examination of each nanostructure's geometry [127]. Measurement errors increase significantly for smaller NWs, potentially causing overestimations of the elastic modulus, which might be misinterpreted as a "size effect" [77]. The onset diameter of this effect,

where surface contributions become significant, is around 10-40 nm, but most NWs in this study were above 50 nm, minimizing this issue [77,128].

Point defects, such as oxygen vacancies, can elongate bond lengths and decrease the elastic modulus [60,61,128,129]. For example, ZnO NWs and Al_2O_3 nanobelts with higher oxygen vacancy densities exhibited up to 20% and 16% lower Young's modulus, respectively [130,131]. Similarly, as-grown Ga_2O_3 NWs showed lower elastic modulus values due to significant oxygen vacancies [132]. Planar defects like stacking faults also impact mechanical properties, with some studies reporting reductions in Young's modulus up to tenfold [133-136].

Variations in measured elastic moduli are linked to cross-section geometry and growth directions, but the significant decrease compared to bulk values remains unclear. Previous studies suggested high oxygen vacancy concentrations could contribute to lower elastic modulus values [132]. TEM studies did not reveal stacking faults, which might enhance elasticity. Further research using advanced methods like *in situ* TEM mechanical resonance is needed to fully understand the factors influencing the elastic properties of Ga_2O_3 NWs, including geometry, crystalline orientation, and planar defects.

5.3. Heat-induced fragmentation and adhesive behaviour of Au nanowires

In this section, the effect of heating schemes and temperature on the formation of Au NW fragments, along with the adhesive behaviour of NPs produced through this approach, was investigated. Additionally, the feasibility of heat-induced Au NW fragmentation for patterned SERS substrate was evaluated. The findings presented in this section have been published in **Paper III**.

5.3.1. Thermal annealing of Au nanowires

The thermal behaviour of NWs was explored through controlled heating processes using a laboratory furnace. Au NWs underwent two distinct heating schemes to understand their response to temperature changes and structural alterations. In the **first scheme**, the same NW sample was gradually heated from 300°C to 600°C in 50°C increments, with each temperature step lasting 30 minutes. The NW sample was placed into the furnace once it had been heated to the desired temperature. Following each heating cycle, samples were taken out of furnace, cooled down and SEM imaging was performed to examine the sample. The **second scheme** involved rapid heating, utilizing a fresh sample for each experiment to accurately determine the temperature at which fragmentation

begins. Heating was conducted between 300°C and 600°C, each for a duration of 30 minutes.

A controlled gradual heating process was applied to the same NW sample (see *Figure 5.11*), raising the temperature from 300°C to 600°C in 50°C increments and maintaining a consistent duration of 30 minutes at each temperature step (the first heating scheme). In the SEM micrographs provided, it is apparent that both the nanorods (NRs) and NWs demonstrate a tendency to decrease in length and increase in width due to the diffusion of Au atoms. Notably, visible alterations in morphology are observed in both types of nanostructures at 400°C. The temperature range spanning from 400°C to 500°C represents a period of particularly rapid transformations in both NRs and NWs.

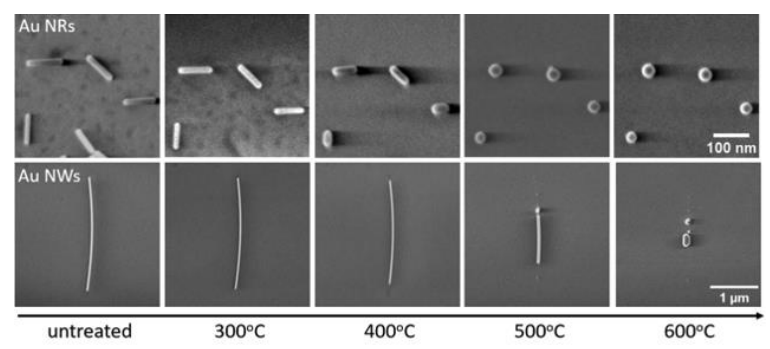


Figure 5.11. SEM micrographs of untreated and gradually thermally annealed (first heating scheme) Au NRs and NWs.

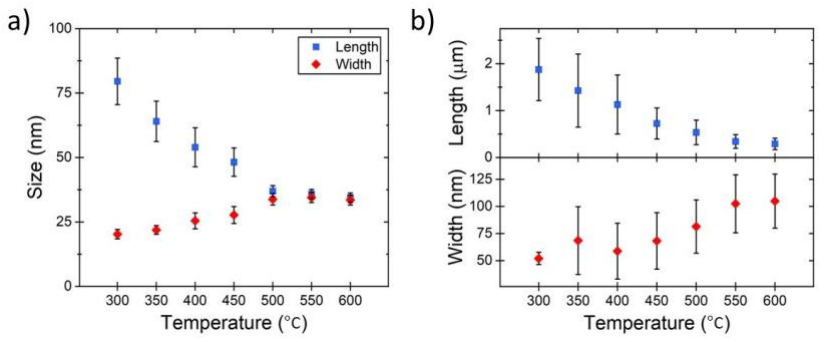


Figure 5.12. Change in particle size depending on the heating temperature for: (a) Au NRs; (b) Au NWs.

For statistical validity, nanostructure dimensions were measured systematically after each heating cycle (the first heating scheme). Analysis (see

Figure 5.12) revealed that as heating temperature increased gradually, nanostructure length decreased while width increased. Around 550°C, both NRs and NWs showed a tendency to transition into more thermodynamically stable states, forming nanospheres. NWs, with higher aspect ratios due to significant length-to-width ratios, retained their original structure and shape at lower temperatures, with atoms constrained to vibrational motion. However, above 500°C, diffusive activities of surface atoms became significant, facilitating rearrangement and diffusion into a spherical configuration. This transformation occurred over time with the first heating scheme.

The second heating scheme aimed to explore the fragmentation behaviour of Au NWs under different temperature conditions. Fragmentation of metal NWs into shorter segments at elevated temperatures is a well-known phenomenon referred to as Rayleigh instability. This process occurs through the diffusion of surface atoms and is driven by the minimization of surface energy, leading to the formation of faceted fragments predominantly bounded by {111} surfaces. Initially, the surfaces of pentagonal Au wires are {100}, but they transition to the more energetically favorable {111} surfaces at the wire ends. Consequently, the NW breaks into multiple fragments or NRs. Previous experiments have indicated that gradual heating allows more time for diffusion-induced shape changes, resulting in NWs transforming into nanospheres instead of fragmenting into several pieces. As depicted in *Figure 5.13*, it is evident that when rapidly heated to 600°C for 30 minutes using the second scheme, Au NWs are fragmented into smaller segments, exhibiting periodic spacing between these fragmented sections.

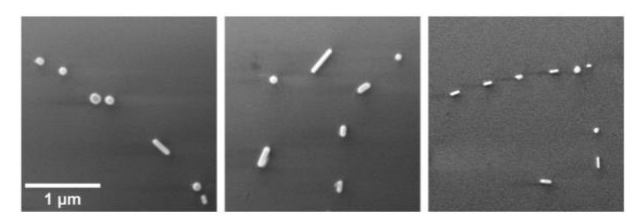


Figure 5.13. SEM micrographs of rapidly heated (the second heating scheme) NWs at 600°C for 30 min.

5.3.2. AFM measurements

Exploring the creation of robust SERS substrates requires ensuring strong adhesion of NPs to the substrate surface, preventing their displacement or removal by dye-containing solutions. In this regard, AFM manipulations were employed to assess whether the NPs, produced through the second heating

scheme at 600° C, achieved sufficient adhesion to the substrate. The mobility of the Au NPs was evaluated by measuring the power dissipated in tapping-mode AFM, a technique previously demonstrated to be effective for assessing NP mobility. The heat-induced rounding of NPs is expected to reduce the contact area, thereby decreasing friction forces, in line with the established relationship $\tau = F/A$, where τ represents contact strength, F denotes friction force, and A signifies contact area. A total of over 400 Au NPs were measured, and approximately 83.7% of these NPs showed no mobility under AFM manipulations. In *Figure 5.14*, the topography images depict the changes in fragmented Au NWs on the Si substrate before (see *Figure 5.14(a)*) and after (see *Figure 5.14(b)*) AFM manipulations, illustrating the impact of manipulations on NP arrangement and adhesion. The median power dissipated for moving a NP was 0.13 pW. These results underscore the efficacy of the proposed fabrication approach in producing stable SERS substrates with well-adhered NPs.

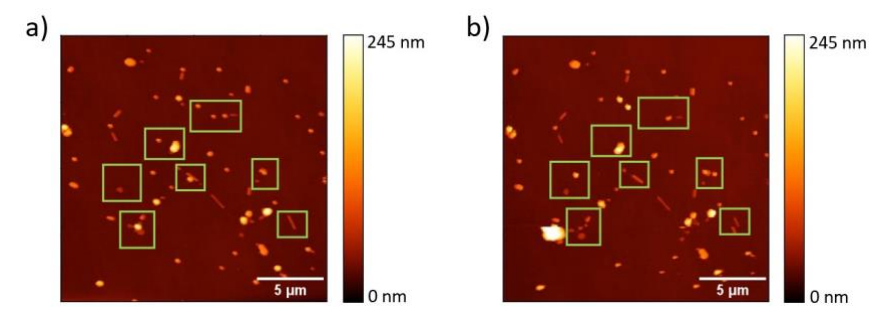


Figure 5.14. A topography image shows a $20\times20~\mu m$ region of thermally annealed (600°C) Au NWs on the Si substrate: (a) before AFM manipulations; (b) after AFM manipulations. The green frames highlight the areas where NP displacement occurred.

5.3.3. Raman measurements

Raman measurements of Rhodamine B molecules adsorbed on a Si wafer surface were explored using Au NWs and NRs before and after thermal annealing (see *Figure 5.15*). Despite optimizing the excitation wavelength for Rhodamine B, no significant Raman peaks associated with it were detected on the bare Si wafer surface. To enhance the Raman signal of Rhodamine B, Au NWs and NRs before and after thermal annealing at 600°C were introduced onto the Si wafer surface. Substrates with as-prepared Au NRs and NWs displayed the main SERS peaks of Rhodamine B at 621, 1278, 1356, 1507, and 1526 cm⁻¹. Measurements for substrates with thermally annealed NRs and NWs showed an

increased Raman signal for Rhodamine B, evident from the amplified Raman peaks observed in the spectra. Raman spectra of the heated NWs exhibited significantly higher intensities compared to the heated NRs. Calculated EFs showed a substantial improvement through annealing at 600°C. Specifically, the EF for Au NRs increased from 3.8×10^5 to 8.3×10^5 after annealing, while for annealed Au NWs, it reached 1.6×10^6 , representing nearly a 30-fold increase compared to unannealed NWs with an EF of 5.5×10^4 .

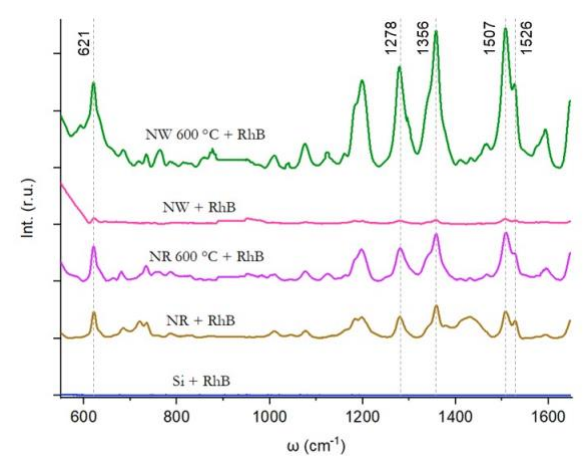


Figure 5.15. Raman scattering from Rhodamine B molecules on an oxidized Si wafer in the presence of untreated and thermally treated Au nanostructures.

The EF for NRs was 7 times higher than NWs before annealing. The initial average diameter of NWs was nearly three times larger than NRs. After annealing, both NP types increased in diameter, enhancing the Raman signal. Post-annealing, NWs were about twice as efficient for SERS enhancement compared to NRs, likely due to their larger diameter. Thermal annealing of Au NRs produced larger, more distributed nanospheres, while rapid NW annealing at higher temperatures created more patterned NPs. The data suggests shape and size are key factors for the SERS effect, consistent with previous literature [137,138].

5.4. Heat-induced morphological changes in Ag nanowires

In this section, the experimental outcomes of the Ag NWs deposited onto specially patterned Si substrates and subsequent heating of the samples to

various temperatures in an air environment are presented. The contrasting behaviours between the suspended and adhered parts of Ag NWs during heating are examined. The findings presented in this section have been published in **Paper IV**.

5.4.1. Heat treatment of the Ag nanowires

The thermal behaviour of Ag NWs was explored through controlled heating processes using a laboratory furnace. Two heating schemes were employed in this study. **Scheme 1** involved heating in 10-minute cycles at fixed temperatures followed by cooling to room temperature. The initial cycle commenced at 100°C, with subsequent increments of 50°C until reaching 200°C. Further temperature increases were set at 25°C intervals until reaching 450°C. **Scheme 2** entailed heating freshly made samples in a single step for 10 minutes at a target temperature determined based on the results obtained from Scheme 1.

5.4.2. First heating scheme

There were no observable alterations in the morphology of Ag NWs at heat-treatment temperatures up to 275 °C. However, at 300 °C and above, initial signs of diffusion in NWs became apparent, characterized by splitting at locations where NWs were partially fractured during deposition (refer to *Figure 5.16*). At this stage, there was no observable distinction in the behaviour of adhered and suspended parts of NWs concerning structural integrity. The primary influential factor observed in the process was the diameter of the NWs.

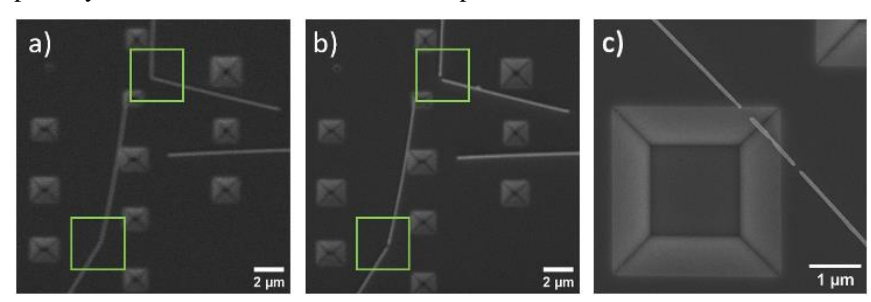


Figure 5.16. SEM micrographs of: (a) Ag NWs exhibited deformation upon deposition onto the Si substrate; (b) splitting of the Ag NWs occurred at the bending areas following four heating cycles (100, 150, 200, and 225°C) in Scheme 1; (c) Splitting and necking of Ag NWs in the Scheme 1 after treatment at 375°C.

Between 350° C and 375° C, many Ag NWs exhibited necking and complete splitting approximately in the middle of their suspended segments (see *Figure 5.16(c)*). Beyond 400° C, fragmentation extended to the adhered parts. This observation suggests that in heating Scheme 1, the adhered portions demonstrate greater heat resistance, enduring temperatures around 50° C higher before fragmentation occurs compared to the suspended segments. By 450° C, most NWs experienced splitting in their suspended sections, with extensive fragmentation also evident in the adhered segments. Thinner NWs generally displayed a higher susceptibility to necking and splitting, while thicker NWs exhibited greater resistance to elevated temperatures.

5.4.3. Second heating scheme

In Scheme 2, the initial stage of NW fragmentation was observed, particularly significant for analysing the response of adhered and suspended sections to heat treatment, within the temperature range of 375-400°C. Contrary to observations in Scheme 1, the behaviour of partially suspended NWs in Scheme 2 displayed a distinct pattern. Specifically, extensive fragmentation occurred in the adhered portions while the suspended segments remained intact (see *Figure 5.17*). This phenomenon was most prominent in samples treated at 400°C, thus this temperature was selected for further investigation. Beyond this temperature, widespread fragmentation was observed in both adhered and suspended regions.

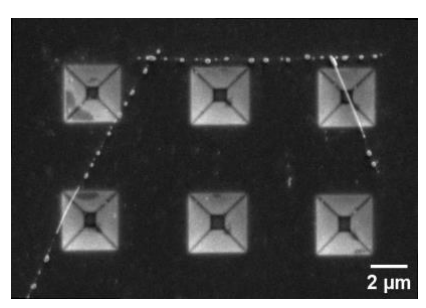


Figure 5.17. SEM image depicting Ag NWs following a single-step heat treatment (Scheme 2) at 400°C. Fragmentation of the NWs predominantly occurred within the adhered sections.

The heat-treatment experiments, repeated twice with freshly prepared samples under both heating schemes, consistently showed splitting tendency. In heating Scheme 1, splitting occurred first in the middle of suspended parts, while in Scheme 2, it occurred in the adhered parts. To quantitatively assess the degree

of splitting in both the adhered and suspended parts of Ag NWs, two parameters were introduced: "splits per part", representing the total number of split events separately for the adhered and suspended parts of each NW, and "splits per unit length", indicating the number of split events per length of either the adhered or suspended part. The number of splits was determined from SEM images of large areas (approximately $120{\times}80~\mu\text{m}$) captured at maximum picture resolution (6144×4415). This approach ensured an unbiased analysis, with all NWs within the large areas being examined. Subsequently, average values for all analysed NWs were calculated separately for each heating scheme. In total, 111 adhered parts and 101 suspended parts were analysed for heating Scheme 1, and 87 adhered parts and 64 suspended parts for heating Scheme 2. In heating Scheme 1, the extent of fragmentation in the suspended parts is one order of magnitude higher than that in the adhered parts, while the opposite behaviour is observed for the second heating scheme.

5.4.4. Inner structure of Ag nanowires

The Ag NWs used in this investigation exhibit a five-fold twinned crystal configuration, resulting in a pentagonal cross-sectional shape [139]. This pentagonal symmetry, considered a "forbidden" pattern in crystallography, inherently induces internal strains within the structure. These strains may act as a potential driving force leading to the heat-induced fragmentation of Ag NWs, serving as a mechanism for stress release and possibly involving recrystallization into single crystals. To assess this hypothesis, further experiments were conducted using TEM grids, allowing for the observation of the crystal structure in TEM. Remarkably, it was observed that even in the case of small fragments resulting from heat treatment, the pentagonal structure remained intact, as illustrated in *Figure 5.18*.

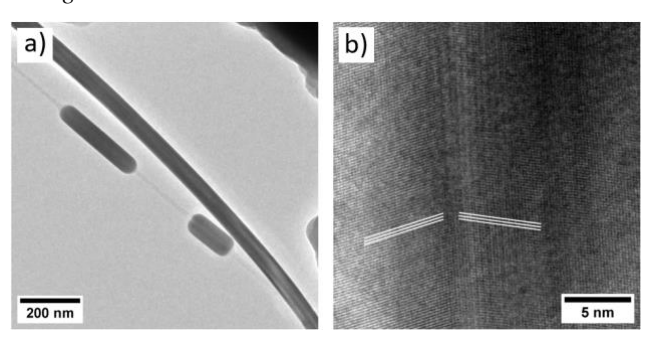


Figure 5.18. TEM micrographs of: (a) Ag NWs post single-step (Scheme 2) heat treatment; (b) inset highlighting one of the segments. The dark lines observed in

the middle of the NWs correspond to a twin boundary between two crystal segments.

It is noteworthy that the fragments remained in position due to contact with the thin carbon membrane of the TEM grid. This discovery suggests that the morphological alterations induced by heat in Ag NWs occur through surface diffusion mechanisms without compromising the crystal structure.

5.4.5. Mechanisms behind the heat-induced Ag nanowire splitting

Given the findings, critical factors affecting the outcomes of heattreatment investigations include the substantially higher thermal expansion coefficient of Ag compared to Si (18.9 vs 2.8×10-6 m/(m°C)), and previous studies by Vlassov et al. [140] indicating strong bonding between Ag NWs and Si substrates. These factors suggest that thermal expansion of Ag NWs could induce significant mechanical stresses within the NWs, particularly at the interface with the Si substrate, potentially leading to the redistribution of Ag atoms and splitting of the NWs to relieve stress. FEM simulations conducted in collaboration with the Institute of Technology at the University of Tartu confirmed high stresses at the NW-substrate interface and in the middle of segments. providing qualitative insights thermomechanical phenomena. Repeated heat-induced bending could induce fatigue and defect formation in the suspended segment, increased by heatassisted rearrangement of Ag atoms at the substrate contact. This could lead to defects and necking in the middle of the suspended segment, consistent with experimental observations. Diffusion of atoms away from defect regions may thin the NW, potentially causing splitting before other regions, proposing a mechanism for NW splitting during heat treatment.

In Scheme 2, without heating cycles, the suspended parts are not subjected to repeated compression and tensile stresses. Similar to the general behaviour observed with heated Ag and Au NWs on flat Si substrates [90], the adhered parts split into shorter fragments. This phenomenon is commonly attributed to Rayleigh instability [91,93,141]. The longer endurance of suspended parts in these experiments suggests that interfacial stresses play a significant role in the fragmentation process. Additionally, in certain cases, surviving parts extend beyond the visible suspended portion, possibly due to heat-induced bending.

MD simulations, conducted in collaboration with the Institute of Technology at the University of Tartu, aimed to explore stress-induced impact of defects on NW splitting in Scheme 1. Using a simplified model of a periodic prismatic rod with a five-fold twinned inner structure, heating and cooling cycles

induced defect formation and amorphous regions, leading to necking and splitting.

CONCLUSIONS

In this Dissertation, the main objective was to investigate mechanical and thermal behaviours of selected material NWs using electron microscopy nanomanipulation techniques and heating experiments.

A significant advancement in the field was achieved with the first observation of mechanically induced post-synthesis kinking in non-metallic NWs. Through three different manipulation scenarios and MD calculations, the mechanical induction of kinking and unkinking in CuO NWs was successfully demonstrated. Structural analyses using high-resolution TEM and SAED, alongside kinking angle measurements, revealed that the observed kinking in CuO NWs corresponds to twinning along the (Π 0) crystal plane of CuO. The findings suggest that deformation twinning may occur when external forces are applied in a specific direction. This newly discovered phenomenon opens a new route for research into post-synthesis modifications of other non-metallic NWs.

The experimental determination of the elastic moduli of individual $\beta\text{-}Ga_2O_3\,$ NWs using both three-point bending and mechanical resonance techniques revealed significant scattering in the obtained data. The mean values obtained were 34.5 GPa from resonance and 75.8 GPa from three-point bending methods, highlighting the challenges posed by variations in cross-section geometry and the presence of different growth directions of the $Ga_2O_3\,$ NWs. The observed scattering of the values of elastic moduli of individual $\beta\text{-}Ga_2O_3\,$ NWs underscores the necessity for precisely controlled synthesis methods for $\beta\text{-}Ga_2O_3\,$ NWs and thorough post-examination of their mechanical properties.

Significant differences in the thermal behaviour and structural transformations of Au NWs were observed between the two heating schemes, with the gradual heating method showing morphological changes without fragmentation, whereas the rapid heating method led to fragmentation and the formation of nanospheres and nanorods at elevated temperatures, highlighting the effectiveness of rapid heating for inducing fragmentation in Au NWs. These findings highlight the effectiveness of using fragmented Au NWs in applications such as SERS substrates.

Heat treatment-induced fragmentation of Ag NWs revealed distinct fragmentation patterns depending on the method of temperature increase, with NWs splitting primarily in suspended parts at 375°C in rapid cycles and fragmentation occurring mainly in adhered parts under direct temperature increase, highlighting the role of substrate interaction in the fragmentation process. Experimental observations, supported by simulations, demonstrated that thermal expansion and frictional forces contribute to the fragmentation of pentagonal Ag NWs, with fragmentation occurring at temperatures exceeding

 400° C, suggesting that heat-induced NW fragmentation involves substrate interaction beyond Rayleigh instability. Continuous research into metal NW fragmentation under varying conditions and substrates could enhance control in cost-effective production methods for applications involving metal nanostructure arrays.

To sum up, the mechanical properties and thermal behaviour of NWs were investigated. Through manipulation techniques and heating experiments, significant advancements were made in understanding the structural transformations and heat-induced behaviour of NWs. These findings underscore the crucial role of manipulation methods and substrate interactions in determining the properties of nanostructures, essential for their potential applications.

PARTICIPATION IN SUMMER SCHOOLS AND CONFERENCES

Summer schools and courses:

- 1. Summer school "European School on Nanosciences & Nanotechonologies (ESONN)", Grenoble, France, 27th of August 9th of September, 2023.
- 2. Summer school "Training School on the MecaNano challenges", Rome, Italy, 24-28th of July, 2023.
- 3. Royal Microscopy Society "Electron Microscopy Spring School", Leeds, UK, 17-21st of April, 2023.
- 4. FM&NT-NIBS 2022 summer school "Advanced topics on material spectroscopy and morphology", Riga, Latvia, 2-3rd of June, 2022.
- 5. Online European course for PhD students and young researchers "HERCULES European School 2022", 28th of February 1st of April, 2022.
- 6. Online summer school "Micro- and nanofabrication of electronic and photonic devices", LU CFI, RISE and KTH, 17-18th of June, 2021.

Conferences:

- International conference "9th European Nanomanipulation Workshop". Poster presentation: "Elastic Modulus of β-Ga₂O₃ Nanowires Measured by Resonance and Three-Point Bending Techniques", Madrid, Spain, 17-19th of June, 2024.
- 2. The 40th Scientific Conference of the Institute of Solid State Physics, University of Latvia. Oral presentation: "Reshaping covalent nanowires by exploiting an unexpected plasticity mediated by deformation twinning", Riga, Latvia. 5-7th of March, 2024.
- International conference "EMRS Fall Meeting 2023". Poster presentation: "Heat-induced Fragmentation of Gold Nanowires for Surface Enhanced Raman Scattering Substrates", Warsaw, Poland. 18-21st of September, 2023.
- 4. International conference "EMRS Fall Meeting 2022". Poster presentation: "Au nanoparticle covered ZnO nanostructure substrates for SERS application", Warsaw, Poland. 19-22nd of September, 2022.
- "Joint International Conference 'Functional Materials and Nanotechnologies' and 'Nanotechnology and Innovation in the Baltic Sea region' - FM&NT – NIBS 2022". Poster presentation: "SERS substrates based on gold nanoparticle-coated ZnO tetrapods", Riga, Latvia. 3-6th of June, 2022.
- International conference "XXV General Assembly and Congress of the International Union of Crystallography - IUCr 2021", Prague, Czech Republic, 14-22th of August, 2021.

REFERENCES

- [1] W. L. F. Armarego, "Nanomaterials," in *Purification of Laboratory Chemicals*, Elsevier, 2022, pp. 586–630. doi: 10.1016/B978-0-323-90968-6.50005-9.
- [2] N. Baig, I. Kammakakam, and W. Falath, "Nanomaterials: a review of synthesis methods, properties, recent progress, and challenges," *Mater Adv*, vol. 2, no. 6, pp. 1821–1871, 2021, doi: 10.1039/D0MA00807A.
- [3] B. Mekuye and B. Abera, "Nanomaterials: An overview of synthesis, classification, characterization, and applications," *Nano Select*, vol. 4, no. 8, pp. 486–501, Aug. 2023, doi: 10.1002/nano.202300038.
- [4] P. C. McIntyre and A. Fontcuberta i Morral, "Semiconductor nanowires: to grow or not to grow?," *Mater Today Nano*, vol. 9, p. 100058, Mar. 2020, doi: 10.1016/j.mtnano.2019.100058.
- [5] K. Liu, B. Ouyang, X. Guo, Y. Guo, and Y. Liu, "Advances in flexible organic field-effect transistors and their applications for flexible electronics," *npj Flexible Electronics*, vol. 6, no. 1, p. 1, Jan. 2022, doi: 10.1038/s41528-022-00133-3.
- [6] S. Wang, Z. Shan, and H. Huang, "The Mechanical Properties of Nanowires," Advanced Science, vol. 4, no. 4, Apr. 2017, doi: 10.1002/advs.201600332.
- [7] W. Lu and C. M. Lieber, "Semiconductor nanowires," J Phys D Appl Phys, vol. 39, no. 21, pp. R387–R406, Nov. 2006, doi: 10.1088/0022-3727/39/21/R01.
- [8] R. Sondors *et al.*, "Size Distribution, Mechanical and Electrical Properties of CuO Nanowires Grown by Modified Thermal Oxidation Methods," *Nanomaterials*, vol. 10, no. 6, p. 1051, May 2020, doi: 10.3390/nano10061051.
- [9] P. Guan *et al.*, "Performance degradation and mitigation strategies of silver nanowire networks: a review," *Critical Reviews in Solid State and Materials Sciences*, vol. 47, no. 3, pp. 435–459, May 2022, doi: 10.1080/10408436.2021.1941753.
- [10] H. Li, J. M. Biser, J. T. Perkins, S. Dutta, R. P. Vinci, and H. M. Chan, "Thermal stability of Cu nanowires on a sapphire substrate," *J Appl Phys*, vol. 103, no. 2, Jan. 2008, doi: 10.1063/1.2837053.
- [11] M. Byakodi *et al.*, "Emerging 0D, 1D, 2D, and 3D nanostructures for efficient point-of-care biosensing," *Biosens Bioelectron X*, vol. 12, p. 100284, Dec. 2022, doi: 10.1016/j.biosx.2022.100284.
- [12] S. A. Afolalu, S. B. Soetan, S. O. Ongbali, A. A. Abioye, and A. S. Oni, "Morphological characterization and physio-chemical properties of nanoparticle review," *IOP Conf Ser Mater Sci Eng*, vol. 640, no. 1, p. 012065, Nov. 2019, doi: 10.1088/1757-899X/640/1/012065.
- [13] N. Joudeh and D. Linke, "Nanoparticle classification, physicochemical properties, characterization, and applications: a comprehensive review for biologists," J Nanobiotechnology, vol. 20, no. 1, p. 262, Jun. 2022, doi: 10.1186/s12951-022-01477-8.
- [14] M. Velický and R. A. W. Dryfe, "Electrochemistry of 2D nanomaterials," 2021, pp. 485–536. doi: 10.1016/B978-0-12-820055-1.00009-5.
- [15] C. Verma, E. Berdimurodov, D. K. Verma, K. Berdimuradov, A. Alfantazi, and C. M. Hussain, "3D Nanomaterials: The future of industrial, biological, and environmental applications," *Inorg Chem Commun*, vol. 156, p. 111163, Oct. 2023, doi: 10.1016/j.inoche.2023.111163.
- [16] A. G. N. Sofiah, M. Samykano, K. Kadirgama, R. V. Mohan, and N. A. C. Lah, "Metallic nanowires: Mechanical properties Theory and experiment," *Appl Mater Today*, vol. 11, pp. 320–337, Jun. 2018, doi: 10.1016/j.apmt.2018.03.004.
- [17] C.-Y. Hsu *et al.*, "Nanowires Properties and Applications: A Review Study," *S Afr J Chem Eng*, vol. 46, pp. 286–311, Oct. 2023, doi: 10.1016/j.sajce.2023.08.006.

- [18] D. W. Hobson, "Nanotechnology," in *Comprehensive Biotechnology*, Elsevier, 2011, pp. 683–697. doi: 10.1016/B978-0-08-088504-9.00228-2.
- [19] N. P. Dasgupta et al., "25th Anniversary Article: Semiconductor Nanowires Synthesis, Characterization, and Applications," Advanced Materials, vol. 26, no. 14, pp. 2137–2184, Apr. 2014, doi: 10.1002/adma.201305929.
- [20] M. Nehra et al., "1D semiconductor nanowires for energy conversion, harvesting and storage applications," Nano Energy, vol. 76, p. 104991, Oct. 2020, doi: 10.1016/j.nanoen.2020.104991.
- [21] W. Lu and C. M. Lieber, "Semiconductor nanowires," J Phys D Appl Phys, vol. 39, no. 21, pp. R387–R406, Nov. 2006, doi: 10.1088/0022-3727/39/21/R01.
- [22] Y.-Z. Long, M. Yu, B. Sun, C.-Z. Gu, and Z. Fan, "Recent advances in large-scale assembly of semiconducting inorganic nanowires and nanofibers for electronics, sensors and photovoltaics," *Chem Soc Rev*, vol. 41, no. 12, p. 4560, 2012, doi: 10.1039/c2cs15335a.
- [23] S. Vlassov, S. Oras, B. Polyakov, E. Butanovs, A. Kyritsakis, and V. Zadin, "Kinking in Semiconductor Nanowires: A Review," *Cryst Growth Des*, vol. 22, no. 1, pp. 871–892, Jan. 2022, doi: 10.1021/acs.cgd.1c00802.
- [24] J. G. Lu, P. Chang, and Z. Fan, "Quasi-one-dimensional metal oxide materials—Synthesis, properties and applications," *Materials Science and Engineering: R: Reports*, vol. 52, no. 1–3, pp. 49–91, May 2006, doi: 10.1016/j.mser.2006.04.002.
- [25] B. Alhalaili et al., "Gallium oxide nanowires for UV detection with enhanced growth and material properties," Sci Rep, vol. 10, no. 1, p. 21434, Dec. 2020, doi: 10.1038/s41598-020-78326-x.
- [26] M. Higashiwaki, "β-Ga2O3 material properties, growth technologies, and devices: a review," AAPPS Bulletin, vol. 32, no. 1, p. 3, Jan. 2022, doi: 10.1007/s43673-021-00033-0.
- [27] E. Butanovs, L. Dipane, A. Zolotarjovs, S. Vlassov, and B. Polyakov, "Preparation of functional Ga2S3 and Ga2Se3 shells around Ga2O3 nanowires via sulfurization or selenization," Opt. Mater. (Amst.), vol. 131, p. 112675, Sep. 2022, doi: 10.1016/j.optmat.2022.112675.
- [28] S. J. Pearton *et al.*, "A review of Ga2O3 materials, processing, and devices," *Appl Phys Rev*, vol. 5, no. 1, Mar. 2018, doi: 10.1063/1.5006941.
- [29] C. Sivakumar, G.-H. Tsai, P.-F. Chung, B. Balraj, Y.-F. Lin, and M.-S. Ho, "High-Quality Single-Crystalline β-Ga2O3 Nanowires: Synthesis to Nonvolatile Memory Applications," *Nanomaterials*, vol. 11, no. 8, p. 2013, Aug. 2021, doi: 10.3390/nano11082013.
- [30] B. Alhalaili et al., "Gallium oxide nanowires for UV detection with enhanced growth and material properties," Sci Rep, vol. 10, no. 1, p. 21434, Dec. 2020, doi: 10.1038/s41598-020-78326-x.
- [31] A.-C. Liu *et al.*, "State-of-the-Art β-Ga 2 O 3 Field-Effect Transistors for Power Electronics," *ACS Omega*, vol. 7, no. 41, pp. 36070–36091, Oct. 2022, doi: 10.1021/acsomega.2c03345.
- [32] Y. Li *et al.*, "Efficient Assembly of Bridged β -Ga 2 O 3 Nanowires for Solar-Blind Photodetection," *Adv Funct Mater*, vol. 20, no. 22, pp. 3972–3978, Nov. 2010, doi: 10.1002/adfm.201001140.
- [33] D. Guo, Q. Guo, Z. Chen, Z. Wu, P. Li, and W. Tang, "Review of Ga2O3-based optoelectronic devices," *Materials Today Physics*, vol. 11, p. 100157, Dec. 2019, doi: 10.1016/j.mtphys.2019.100157.
- [34] M. Zhang *et al.*, "β-Ga2O3-Based Power Devices: A Concise Review," *Crystals (Basel)*, vol. 12, no. 3, p. 406, Mar. 2022, doi: 10.3390/cryst12030406.
- [35] A. Afzal, "β-Ga2O3 nanowires and thin films for metal oxide semiconductor gas sensors: Sensing mechanisms and performance enhancement strategies," *Journal of Materiomics*, vol. 5, no. 4, pp. 542–557, Dec. 2019, doi: 10.1016/j.jmat.2019.08.003.

- [36] S. Cui, Z. Mei, Y. Zhang, H. Liang, and X. Du, "Room-Temperature Fabricated Amorphous Ga 2 O 3 High-Response-Speed Solar-Blind Photodetector on Rigid and Flexible Substrates," Adv Opt Mater, vol. 5, no. 19, Oct. 2017, doi: 10.1002/adom.201700454.
- [37] S. Wang *et al.*, "In situ synthesis of monoclinic β-Ga2O3 nanowires on flexible substrate and solar-blind photodetector," *J Alloys Compd*, vol. 787, pp. 133–139, May 2019, doi: 10.1016/j.jallcom.2019.02.031.
- [38] Min-Feng Yu, M. Z. Atashbar, and X. Chen, "Mechanical and electrical characterization of /spl beta/-Ga/sub 2/O/sub 3/ nanostructures for sensing applications," *IEEE Sens J*, vol. 5, no. 1, pp. 20–25, Feb. 2005, doi: 10.1109/JSEN.2004.838669.
- [39] M.-S. Jo et al., "Aligned CuO nanowire array for a high performance visible light photodetector," Sci Rep, vol. 12, no. 1, p. 2284, Feb. 2022, doi: 10.1038/s41598-022-06031-y.
- [40] R. Sondors et al., "Size Distribution, Mechanical and Electrical Properties of CuO Nanowires Grown by Modified Thermal Oxidation Methods," Nanomaterials, vol. 10, no. 6, p. 1051, May 2020, doi: 10.3390/nano10061051.
- [41] B. Polyakov et al., "In situ measurements of ultimate bending strength of CuO and ZnO nanowires," Eur Phys J B, vol. 85, no. 11, p. 366, Nov. 2012, doi: 10.1140/epjb/e2012-30430-6.
- [42] B. Polyakov, S. Vlassov, L. M. Dorogin, P. Kulis, I. Kink, and R. Lohmus, "The effect of substrate roughness on the static friction of CuO nanowires," *Surf Sci*, vol. 606, no. 17–18, pp. 1393–1399, Sep. 2012, doi: 10.1016/j.susc.2012.04.029.
- [43] H. Sheng et al., "Anelasticity of twinned CuO nanowires," Nano Res, vol. 8, no. 11, pp. 3687–3693, Nov. 2015, doi: 10.1007/s12274-015-0868-x.
- [44] S. Lal, J. H. Hafner, N. J. Halas, S. Link, and P. Nordlander, "Noble Metal Nanowires: From Plasmon Waveguides to Passive and Active Devices," *Acc Chem Res*, vol. 45, no. 11, pp. 1887–1895, Nov. 2012, doi: 10.1021/ar300133j.
- [45] M. Antsov et al., "Mechanical characterisation of pentagonal gold nanowires in three different test configurations: A comparative study," *Micron*, vol. 124, p. 102686, Sep. 2019, doi: 10.1016/j.micron.2019.102686.
- [46] J. Cai *et al.*, "SERS hotspots distribution of the highly ordered noble metal arrays on flexible substrates," *Opt Mater (Amst)*, vol. 122, p. 111779, Dec. 2021, doi: 10.1016/j.optmat.2021.111779.
- [47] I. Yoon *et al.*, "Single Nanowire on a Film as an Efficient SERS-Active Platform," *J Am Chem Soc*, vol. 131, no. 2, pp. 758–762, Jan. 2009, doi: 10.1021/ja807455s.
- [48] M. Arefpour, M. Almasi Kashi, F. Khansari Barzoki, M. Noormohammadi, and A. Ramazani, "Electrodeposited metal nanowires as transparent conductive electrodes: Their release conditions, electrical conductivity, optical transparency and chemical stability," *Mater Des*, vol. 157, pp. 326–336, Nov. 2018, doi: 10.1016/j.matdes.2018.07.048.
- [49] X. Lu, Y. Zhang, and Z. Zheng, "Metal-Based Flexible Transparent Electrodes: Challenges and Recent Advances," Adv Electron Mater, vol. 7, no. 5, May 2021, doi: 10.1002/aelm.202001121.
- [50] J. Choi, G. Sauer, K. Nielsch, R. B. Wehrspohn, and U. Gösele, "Hexagonally Arranged Monodisperse Silver Nanowires with Adjustable Diameter and High Aspect Ratio," *Chemistry of Materials*, vol. 15, no. 3, pp. 776–779, Feb. 2003, doi: 10.1021/cm0208758.
- [51] S. G. Nuriyeva, H. A. Shirinova, K. M. Hasanov, and F. V. Hajiyeva, "Controlled Synthesis of Silver Nanowires: Production and Characterization," *Acta Phys Pol A*, vol. 143, no. 4, pp. 279–283, Apr. 2023, doi: 10.12693/APhysPolA.143.279.
- [52] C. Celle, C. Mayousse, E. Moreau, H. Basti, A. Carella, and J.-P. Simonato, "Highly flexible transparent film heaters based on random networks of silver nanowires," *Nano Res*, vol. 5, no. 6, pp. 427–433, Jun. 2012, doi: 10.1007/s12274-012-0225-2.

- [53] A. Diaz-Alvarez et al., "Emergent dynamics of neuromorphic nanowire networks," Sci Rep., vol. 9, no. 1, p. 14920, Oct. 2019, doi: 10.1038/s41598-019-51330-6.
- [54] H. H. Khaligh and I. A. Goldthorpe, "Failure of silver nanowire transparent electrodes under current flow," *Nanoscale Res Lett*, vol. 8, no. 1, p. 235, Dec. 2013, doi: 10.1186/1556-276X-8-235.
- [55] D. P. Langley et al., "Metallic nanowire networks: effects of thermal annealing on electrical resistance," Nanoscale, vol. 6, no. 22, pp. 13535–13543, 2014, doi: 10.1039/C4NR04151H.
- [56] H. Li, J. M. Biser, J. T. Perkins, S. Dutta, R. P. Vinci, and H. M. Chan, "Thermal stability of Cu nanowires on a sapphire substrate," *J Appl Phys*, vol. 103, no. 2, Jan. 2008, doi: 10.1063/1.2837053.
- [57] A. L. Goodwin, "Opportunities and challenges in understanding complex functional materials," *Nat Commun*, vol. 10, no. 1, p. 4461, Oct. 2019, doi: 10.1038/s41467-019-12422-z.
- [58] "doitpoms." [Online]. Available: https://www.doitpoms.ac.uk/tlplib/atomic-scale-structure/printall.php
- [59] W. D. Callister, MATERIALS SCIENCE AND ENGINEERING, 10th ed. Wiley, 2020.
- [60] K. L. Duncan, Y. Wang, S. R. Bishop, F. Ebrahimi, and E. D. Wachsman, "Role of Point Defects in the Physical Properties of Fluorite Oxides," *Journal of the American Ceramic Society*, vol. 89, no. 10, pp. 3162–3166, Oct. 2006, doi: 10.1111/j.1551-2916.2006.01193.x.
- [61] J. Xi, P. Zhang, C. He, H. Zang, D. Guo, and T. Li, "The role of point defects in the swelling and elastic modulus of irradiated cubic silicon carbide," *Nucl Instrum Methods Phys Res* B, vol. 356–357, pp. 62–68, Aug. 2015, doi: 10.1016/j.nimb.2015.04.059.
- [62] L. Li, Z. Zhang, P. Zhang, and Z. Zhang, "A review on the fatigue cracking of twin boundaries: Crystallographic orientation and stacking fault energy," *Prog Mater Sci*, vol. 131, p. 101011, Jan. 2023, doi: 10.1016/j.pmatsci.2022.101011.
- [63] R. Su et al., "The influence of stacking faults on mechanical behavior of advanced materials," Materials Science and Engineering: A, vol. 803, p. 140696, Jan. 2021, doi: 10.1016/j.msea.2020.140696.
- [64] Y. Li, Y. Wang, S. Ryu, A. F. Marshall, W. Cai, and P. C. McIntyre, "Spontaneous, Defect-Free Kinking via Capillary Instability during Vapor–Liquid–Solid Nanowire Growth," *Nano Lett*, vol. 16, no. 3, pp. 1713–1718, Mar. 2016, doi: 10.1021/acs.nanolett.5b04633.
- [65] Z. He, H. T. Nguyen, L. Duc Toan, and D. Pribat, "A detailed study of kinking in indium-catalyzed silicon nanowires," *CrystEngComm*, vol. 17, no. 33, pp. 6286–6296, 2015, doi: 10.1039/C5CE00773A.
- [66] S. Vlassov et al., "Reshaping Covalent Nanowires by Exploiting an Unexpected Plasticity Mediated by Deformation Twinning," Small, vol. 20, no. 1, Jan. 2024, doi: 10.1002/smll.202304614.
- [67] M. Paladugu et al., "Novel Growth Phenomena Observed in Axial InAs/GaAs Nanowire Heterostructures," Small, vol. 3, no. 11, pp. 1873–1877, Nov. 2007, doi: 10.1002/smll.200700222.
- [68] H. Zhao, A. S. Eggeman, C. P. Race, and B. Derby, "Geometrical constraints on the bending deformation of Penta-twinned silver nanowires," *Acta Mater*, vol. 185, pp. 110– 118, Feb. 2020, doi: 10.1016/j.actamat.2019.11.058.
- [69] S. Lee et al., "Reversible cyclic deformation mechanism of gold nanowires by twinning—detwinning transition evidenced from in situ TEM," Nat Commun, vol. 5, no. 1, p. 3033, Jan. 2014, doi: 10.1038/ncomms4033.
- [70] Y. Chen, X. An, and X. Liao, "Mechanical behaviors of nanowires," *Appl Phys Rev*, vol. 4, no. 3, p. 031104, Sep. 2017, doi: 10.1063/1.4989649.

- [71] F. Östlund et al., "Brittle-to-Ductile Transition in Uniaxial Compression of Silicon Pillars at Room Temperature," Adv Funct Mater, vol. 19, no. 15, pp. 2439–2444, Aug. 2009, doi: 10.1002/adfm.200900418.
- [72] Y. Wu, Q. Rao, J. P. Best, D. Mu, X. Xu, and H. Huang, "Superior Room Temperature Compressive Plasticity of Submicron Beta-Phase Gallium Oxide Single Crystals," Adv Funct Mater, vol. 32, no. 48, Nov. 2022, doi: 10.1002/adfm.202207960.
- [73] F. Mignerot, B. Kedjar, H. Bahsoun, and L. Thilly, "Size-induced twinning in InSb semiconductor during room temperature deformation," *Sci Rep*, vol. 11, no. 1, p. 19441, Oct. 2021, doi: 10.1038/s41598-021-98492-w.
- [74] Q. Wu, W. Miao, Y. Zhang, H. Gao, and D. Hui, "Mechanical properties of nanomaterials: A review," *Nanotechnol Rev*, vol. 9, no. 1, pp. 259–273, Mar. 2020, doi: 10.1515/ntrev-2020-0021.
- [75] A. Reghunadhan, N. Kalarikkal, and S. Thomas, "Mechanical Property Analysis of Nanomaterials," in *Characterization of Nanomaterials*, Elsevier, 2018, pp. 191–212. doi: 10.1016/B978-0-08-101973-3.00007-9.
- [76] X.-Q. Zheng, H. Zhao, Z. Jia, X. Tao, and P. X.-L. Feng, "Young's modulus and corresponding orientation in β-Ga2O3 thin films resolved by nanomechanical resonators," Appl Phys Lett, vol. 119, no. 1, Jul. 2021, doi: 10.1063/5.0050421.
- [77] S. Vlassov et al., "Critical review on experimental and theoretical studies of elastic properties of wurtzite-structured ZnO nanowires," *Nanotechnol Rev*, vol. 12, no. 1, Feb. 2023, doi: 10.1515/ntrev-2022-0505.
- [78] P. Zhou, C. Wu, and X. Li, "Three-point bending Young's modulus of nanowires," *Meas Sci Technol*, vol. 19, no. 11, p. 115703, Nov. 2008, doi: 10.1088/0957-0233/19/11/115703.
- [79] B. R. Neugirg, S. R. Koebley, H. C. Schniepp, and A. Fery, "AFM-based mechanical characterization of single nanofibres," *Nanoscale*, vol. 8, no. 16, pp. 8414–8426, 2016, doi: 10.1039/C6NR00863A.
- [80] N. Wu, L. Chen, Q. Wei, Q. Liu, and J. Li, "Nanoscale three-point bending of single polymer/inorganic composite nanofiber," *Journal of the Textile Institute*, vol. 103, no. 2, pp. 154–158, Feb. 2012, doi: 10.1080/00405000.2011.557187.
- [81] L. Jasulaneca et al., "Determination of Young's modulus of Sb 2 S 3 nanowires by in situ resonance and bending methods," Beilstein Journal of Nanotechnology, vol. 7, pp. 278– 283, Feb. 2016, doi: 10.3762/bjnano.7.25.
- [82] B. Polyakov et al., "Some aspects of formation and tribological properties of silver nanodumbbells," Nanoscale Res Lett, vol. 9, no. 1, p. 186, Dec. 2014, doi: 10.1186/1556-276X-9-186.
- [83] S. J. Marshall, S. C. Bayne, R. Baier, A. P. Tomsia, and G. W. Marshall, "A review of adhesion science," *Dental Materials*, vol. 26, no. 2, pp. e11–e16, Feb. 2010, doi: 10.1016/j.dental.2009.11.157.
- [84] A. Trausa et al., "Heat-Induced Fragmentation and Adhesive Behaviour of Gold Nanowires for Surface-Enhanced Raman Scattering Substrates," ChemEngineering, vol. 8, no. 1, p. 15, Jan. 2024, doi: 10.3390/chemengineering8010015.
- [85] P. Wang et al., "The Evolution of Flexible Electronics: From Nature, Beyond Nature, and To Nature," Advanced Science, vol. 7, no. 20, Oct. 2020, doi: 10.1002/advs.202001116.
- [86] S. Vlassov et al., "Adhesion and Mechanical Properties of PDMS-Based Materials Probed with AFM: A Review," REVIEWS ON ADVANCED MATERIALS SCIENCE, vol. 56, no. 1, pp. 62–78, May 2018, doi: 10.1515/rams-2018-0038.
- [87] G. Guisbiers, "Advances in thermodynamic modelling of nanoparticles," Adv Phys X, vol. 4, no. 1, p. 1668299, Jan. 2019, doi: 10.1080/23746149.2019.1668299.
- [88] M. A. Jabbareh, "A unified bond energy model for size-dependent melting temperature of freestanding and embedded nanomaterials," *Solid State Commun*, vol. 355, p. 114923, Nov. 2022, doi: 10.1016/j.ssc.2022.114923.

- [89] B. Polyakov et al., "Comparison of the resistivities of nanostructured films made from silver, copper-silver and copper nanoparticle and nanowire suspensions," Thin Solid Films, vol. 784, p. 140087, Nov. 2023, doi: 10.1016/j.tsf.2023.140087.
- [90] S. Vigonski et al., "Au nanowire junction breakup through surface atom diffusion," Nanotechnology, vol. 29, no. 1, p. 015704, Jan. 2018, doi: 10.1088/1361-6528/aa9a1b.
- [91] M. E. Toimil Molares, A. G. Balogh, T. W. Cornelius, R. Neumann, and C. Trautmann, "Fragmentation of nanowires driven by Rayleigh instability," *Appl Phys Lett*, vol. 85, no. 22, pp. 5337–5339, Nov. 2004, doi: 10.1063/1.1826237.
- [92] S. Oras et al., "The effect of heat treatment on the morphology and mobility of Au nanoparticles," Beilstein Journal of Nanotechnology, vol. 11, pp. 61–67, Jan. 2020, doi: 10.3762/bjnano.11.6.
- [93] H. Oh, J. Lee, and M. Lee, "Transformation of silver nanowires into nanoparticles by Rayleigh instability: Comparison between laser irradiation and heat treatment," *Appl Surf Sci*, vol. 427, pp. 65–73, Jan. 2018, doi: 10.1016/j.apsusc.2017.08.102.
- [94] A. H. Zewail, "Four-Dimensional Electron Microscopy," *Science* (1979), vol. 328, no. 5975, pp. 187–193, Apr. 2010, doi: 10.1126/science.1166135.
- [95] K. Akhtar, S. A. Khan, S. B. Khan, and A. M. Asiri, "Scanning Electron Microscopy: Principle and Applications in Nanomaterials Characterization," in *Handbook of Materials Characterization*, Cham: Springer International Publishing, 2018, pp. 113–145. doi: 10.1007/978-3-319-92955-2_4.
- [96] M. Ezzahmouly et al., "Micro-computed tomographic and SEM study of porous bioceramics using an adaptive method based on the mathematical morphological operations," Heliyon, vol. 5, no. 12, p. e02557, Dec. 2019, doi: 10.1016/j.heliyon.2019.e02557.
- [97] A. Alyamani and O. M., "FE-SEM Characterization of Some Nanomaterial," in *Scanning Electron Microscopy*, InTech, 2012. doi: 10.5772/34361.
- [98] R. F. Egerton, P. Li, and M. Malac, "Radiation damage in the TEM and SEM," *Micron*, vol. 35, no. 6, pp. 399–409, Aug. 2004, doi: 10.1016/j.micron.2004.02.003.
- [99] R. F. Egerton, "The Transmission Electron Microscope," in *Physical Principles of Electron Microscopy*, Cham: Springer International Publishing, 2016, pp. 55–88. doi: 10.1007/978-3-319-39877-8_3.
- [100] D. B. Carter, C.Barry; Williams, Transmission Electron Microscopy; Springer International Publishing, 2016.
- [101] D. Johnson, N. Hilal, and W. R. Bowen, "Basic Principles of Atomic Force Microscopy," in *Atomic Force Microscopy in Process Engineering*, Elsevier, 2009, pp. 1–30. doi: 10.1016/B978-1-85617-517-3.00001-8.
- [102] Y. F. Dufrêne et al., "Imaging modes of atomic force microscopy for application in molecular and cell biology," Nat Nanotechnol, vol. 12, no. 4, pp. 295–307, Apr. 2017, doi: 10.1038/nnano.2017.45.
- [103] N. Wang and X. Zhao, "Atomic Force Microscopy A Powerful Tool for Studying Contact Electrification," Adv Mater Technol, vol. 8, no. 6, Mar. 2023, doi: 10.1002/admt.202201408.
- [104] A. A. G. Requicha et al., "Manipulation of nanoscale components with the AFM: principles and applications," in Proceedings of the 2001 1st IEEE Conference on Nanotechnology. IEEE-NANO 2001 (Cat. No.01EX516), IEEE, pp. 81–86. doi: 10.1109/NANO.2001.966398.
- [105] Hui Xie and S. Régnier, "Development of a Flexible Robotic System for Multiscale Applications of Micro/Nanoscale Manipulation and Assembly," *IEEE/ASME Transactions* on Mechatronics, vol. 16, no. 2, pp. 266–276, Apr. 2011, doi: 10.1109/TMECH.2010.2040483.

- [106] S. Vlassov et al., "Real-time manipulation of gold nanoparticles inside a scanning electron microscope," Solid State Commun, vol. 151, no. 9, pp. 688–692, May 2011, doi: 10.1016/j.ssc.2011.02.020.
- [107] A. I. Denisyuk, A. V. Krasavin, F. E. Komissarenko, and I. S. Mukhin, "Mechanical, Electrostatic, and Electromagnetic Manipulation of Microobjects and Nanoobjects in Electron Microscopes," 2014, pp. 101–140. doi: 10.1016/B978-0-12-800264-3.00003-4.
- [108] R. T. Emelyanov, A. S. Klimov, I. B. Olenev, E. S. Turysheva, and A. I. Avlasevich, "Investigation of the dynamics of the manipulator drive with a stepper motor," *J Phys Conf Ser*, vol. 1515, no. 4, p. 042043, Apr. 2020, doi: 10.1088/1742-6596/1515/4/042043.
- [109] P. Andrey P., I. Vladimir I., and E. Rurik T., "Study of the Dynamics of the Object Control System of Second Order with Respect to the Placements of the Real Poles," *Journal of Siberian Federal University. Engineering & Technologies*, vol. 11, no. 5, pp. 500–511, Aug. 2018, doi: 10.17516/1999-494X-0049.
- [110] "Proquest." [Online]. Available: https://www.proquest.com/openview/cf19b23a715dce8c8a0d36bb599a5785/1?pq-origsite=gscholar&cbl=18750
- [111] X. D. Bai, P. X. Gao, Z. L. Wang, and E. G. Wang, "Dual-mode mechanical resonance of individual ZnO nanobelts," *Appl Phys Lett*, vol. 82, no. 26, pp. 4806–4808, Jun. 2003, doi: 10.1063/1.1587878.
- [112] B. Polyakov *et al.*, "Mechanical properties of sol–gel derived SiO 2 nanotubes," *Beilstein Journal of Nanotechnology*, vol. 5, pp. 1808–1814, Oct. 2014, doi: 10.3762/bjnano.5.191.
- [113] B. Anczykowski, B. Gotsmann, H. Fuchs, J. P. Cleveland, and V. B. Elings, "How to measure energy dissipation in dynamic mode atomic force microscopy," *Appl Surf Sci*, vol. 140, no. 3–4, pp. 376–382, Feb. 1999, doi: 10.1016/S0169-4332(98)00558-3.
- [114] E. Damerchi et al., "Heat-induced morphological changes in silver nanowires deposited on a patterned silicon substrate," *Beilstein Journal of Nanotechnology*, vol. 15, pp. 435–446, Apr. 2024, doi: 10.3762/bjnano.15.39.
- [115] F. Mignerot, B. Kedjar, H. Bahsoun, and L. Thilly, "Size-induced twinning in InSb semiconductor during room temperature deformation," *Sci Rep*, vol. 11, no. 1, p. 19441, Oct. 2021, doi: 10.1038/s41598-021-98492-w.
- [116] P. Uttam, V. Kumar, K.-H. Kim, and A. Deep, "Nanotwinning: Generation, properties, and application," *Mater Des*, vol. 192, p. 108752, Jul. 2020, doi: 10.1016/j.matdes.2020.108752.
- [117] B. Tian, P. Xie, T. J. Kempa, D. C. Bell, and C. M. Lieber, "Single-crystalline kinked semiconductor nanowire superstructures," *Nat Nanotechnol*, vol. 4, no. 12, pp. 824–829, Dec. 2009, doi: 10.1038/nnano.2009.304.
- [118] Z. Jiang, Q. Qing, P. Xie, R. Gao, and C. M. Lieber, "Kinked p-n Junction Nanowire Probes for High Spatial Resolution Sensing and Intracellular Recording," *Nano Lett*, vol. 12, no. 3, pp. 1711–1716, Mar. 2012, doi: 10.1021/nl300256r.
- [119] L. Gan, M. Liao, H. Li, Y. Ma, and T. Zhai, "Geometry-induced high performance ultraviolet photodetectors in kinked SnO 2 nanowires," *J Mater Chem C Mater*, vol. 3, no. 32, pp. 8300–8306, 2015, doi: 10.1039/C5TC01178G.
- [120] J.-W. Jiang and T. Rabczuk, "Mechanical oscillation of kinked silicon nanowires: A natural nanoscale spring," *Appl Phys Lett*, vol. 102, no. 12, Mar. 2013, doi: 10.1063/1.4799029.
- [121] J.-W. Jiang, J.-H. Zhao, and T. Rabczuk, "Size-sensitive Young's modulus of kinked silicon nanowires," *Nanotechnology*, vol. 24, no. 18, p. 185702, May 2013, doi: 10.1088/0957-4484/24/18/185702.
- [122] Y. Jing, C. Zhang, Y. Liu, L. Guo, and Q. Meng, "Mechanical properties of kinked silicon nanowires," *Physica B Condens Matter*, vol. 462, pp. 59–63, Apr. 2015, doi: 10.1016/j.physb.2015.01.018.

- [123] X. Zou, D. Xie, Y. Sun, and C. Wang, "Nanowires mediated growth of β-Ga2O3 nanobelts for high-temperature (> 573 K) solar-blind photodetectors," *Nano Res*, vol. 16, no. 4, pp. 5548–5554, Apr. 2023, doi: 10.1007/s12274-022-5243-0.
- [124] A. S. Grashchenko, S. A. Kukushkin, V. I. Nikolaev, A. V. Osipov, E. V. Osipova, and I. P. Soshnikov, "Study of the Anisotropic Elastoplastic Properties of β-Ga2O3 Films Synthesized on SiC/Si Substrates," *Physics of the Solid State*, vol. 60, no. 5, pp. 852–857, May 2018, doi: 10.1134/S1063783418050104.
- [125] Y. Yao, Y. Sugawara, K. Sasaki, A. Kuramata, and Y. Ishikawa, "Anisotropic mechanical properties of β-Ga2O3 single-crystal measured via angle-dependent nanoindentation using a Berkovich indenter," *J Appl Phys*, vol. 134, no. 21, Dec. 2023, doi: 10.1063/5.0180389.
- [126] M. Nasr Esfahani and B. E. Alaca, "A Review on Size-Dependent Mechanical Properties of Nanowires," *Adv Eng Mater*, vol. 21, no. 8, Aug. 2019, doi: 10.1002/adem.201900192.
- [127] J. Kosmaca et al., "Young's modulus and indirect morphological analysis of Bi 2 Se 3 nanoribbons by resonance measurements," Nanotechnology, vol. 28, no. 32, p. 325701, Aug. 2017, doi: 10.1088/1361-6528/aa79cd.
- [128] S. Vlassov et al., "Complex tribomechanical characterization of ZnO nanowires: nanomanipulations supported by FEM simulations," Nanotechnology, vol. 27, no. 33, p. 335701, Aug. 2016, doi: 10.1088/0957-4484/27/33/335701.
- [129] S. Wang, Z. Shan, and H. Huang, "The Mechanical Properties of Nanowires," Advanced Science, vol. 4, no. 4, Apr. 2017, doi: 10.1002/advs.201600332.
- [130] X. Wang et al., "Growth Conditions Control the Elastic and Electrical Properties of ZnO Nanowires," Nano Lett, vol. 15, no. 12, pp. 7886–7892, Dec. 2015, doi: 10.1021/acs.nanolett.5b02852.
- [131] S. Wang, Q. Huang, Y. Wu, and H. Huang, "Unique structure and surface-related elastic modulus of alumina nanobelts," *Nanotechnology*, vol. 27, no. 47, p. 475701, Nov. 2016, doi: 10.1088/0957-4484/27/47/475701.
- [132] E. Butanovs, M. Zubkins, R. Nedzinskas, V. Zadin, and B. Polyakov, "Comparison of two methods for one-dimensional Ga2O3-ZnGa2O4 core–shell heterostructure synthesis," J Cryst Growth, vol. 618, p. 127319, Sep. 2023, doi: 10.1016/j.jcrysgro.2023.127319.
- [133] S. Dai et al., "Elastic Properties of GaN Nanowires: Revealing the Influence of Planar Defects on Young's Modulus at Nanoscale," Nano Lett, vol. 15, no. 1, pp. 8–15, Jan. 2015, doi: 10.1021/nl501986d.
- [134] K. H. Liu, W. L. Wang, Z. Xu, L. Liao, X. D. Bai, and E. G. Wang, "In situ probing mechanical properties of individual tungsten oxide nanowires directly grown on tungsten tips inside transmission electron microscope," *Appl Phys Lett*, vol. 89, no. 22, Nov. 2006, doi: 10.1063/1.2397547.
- [135] H. Ni and X. D. Li, "Synthesis, Structural and Mechanical Characterization of Amorphous and Crystalline Boron Nanobelts," *Journal of Nano Research*, vol. 1, pp. 10–22, Jan. 2008, doi: 10.4028/www.scientific.net/JNanoR.1.10.
- [136] M. Lucas, W. Mai, R. Yang, Z. L. Wang, and E. Riedo, "Aspect Ratio Dependence of the Elastic Properties of ZnO Nanobelts," *Nano Lett*, vol. 7, no. 5, pp. 1314–1317, May 2007, doi: 10.1021/nl070310g.
- [137] X. X. Han, R. S. Rodriguez, C. L. Haynes, Y. Ozaki, and B. Zhao, "Surface-enhanced Raman spectroscopy," *Nature Reviews Methods Primers*, vol. 1, no. 1, p. 87, Jan. 2022, doi: 10.1038/s43586-021-00083-6.
- [138] H.-L. Wang, E.-M. You, R. Panneerselvam, S.-Y. Ding, and Z.-Q. Tian, "Advances of surface-enhanced Raman and IR spectroscopies: from nano/microstructures to macrooptical design," *Light Sci Appl*, vol. 10, no. 1, p. 161, Aug. 2021, doi: 10.1038/s41377-021-00599-2.

- [139] S. Vlassov, M. Mets, B. Polyakov, J. Bian, L. Dorogin, and V. Zadin, "Abrupt elastic-to-plastic transition in pentagonal nanowires under bending," *Beilstein Journal of Nanotechnology*, vol. 10, pp. 2468–2476, Dec. 2019, doi: 10.3762/bjnano.10.237.
- [140] S. Vlassov, S. Oras, M. Antsov, J. Butikova, R. Lõhmus, and B. Polyakov, "Low-friction nanojoint prototype," *Nanotechnology*, vol. 29, no. 19, p. 195707, May 2018, doi: 10.1088/1361-6528/aab163.
- [141] J.-H. Kim, J. Ma, S. Jo, S. Lee, and C. S. Kim, "Enhancement of Antibacterial Performance of Silver Nanowire Transparent Film by Post-Heat Treatment," *Nanomaterials*, vol. 10, no. 5, p. 938, May 2020, doi: 10.3390/nano10050938.

ACKNOWLEDGEMENTS

I would like to express my sincere gratitude to the following people for their invaluable support and contributions to this Dissertation:

My supervisor Dr. Edgars Butanovs, for his endless support, insightful discussions, valuable suggestions, and understanding. His guidance has been essential throughout this journey.

Dr. Boris Polyakov, for generously sharing his expertise and knowledge of the techniques used in this Dissertation. His example as a curious and dedicated scientist has been truly inspiring.

Dr. Krišjānis Šmits, for his support throughout my doctoral studies.

Dr. Andris Anspoks, for his belief in me and support.

Dr. Sergei Vlassov for his ideas and discussions. I am truly grateful for his inspiration and contributions to my research. He will be dearly missed.

Dr. Sven Oras, for his collaborative work on AFM experiments and PhD-related memes.

Dr. Elyad Damerchi, for his support with experimental data.

Special thanks to Dr. Tauno Tiirats, Prof. Veronika Zadin, and Dr. Andreas Kyritsakis for their contributions to MD modelling and fruitful discussions.

Čiro Federiko Tipaldi, for his assistance with Raman measurements.

My colleagues and work-friends Līga Ignatāne, Edgars Vanags, Reinis Ignatāns, Kārlis Vilks, Kevon Kadiwala, and Aleksejs Zolotarjovs, for scientific discussions and emotional support.

My mother Sandra Šagarova and stepfather Aleksandrs Šagarovs, for their love, care and efforts to understand and support my academic pursuits.

In loving memory of my father, Normunds Trauss, whose endless curiosity influenced me as a child. Though he's not here to see my achievements, his adventurous spirit remains alive in me.

My friends Paula Zariņa-Šteinerte, Laura Mežule, Armands Eglītis, Līga Jasulaņeca and Ieva Rotkovska, for their unwavering support and encouragement throughout this journey. Their friendship has been a source of strength.

I would like to acknowledge financial support from European Regional Development Fund projects Nr. 1.1.1.1/21/A/053 and Nr. 1.1.1.1/21/A/055, European Union's Horizon 2020 Framework Programme H2020-WIDESPREAD-01-2016-2017-TeamingPhase2 under grant agreement No.739508, project CAMART².